UNIVERSITY OF TURKU

AFT-tracks is a tool to analyze the interplay between cell migration and the extracellular matrix

Master’s Degree Program in Biomedical Imaging

Master's thesis

University of Turku

Faculty of Medicine

Institute of Biomedicine

Author(s):

Daniil Iukhtanov

6.5.2026

Turku

Master's thesis

Subject: Biomedical Imaging

Author(s): Daniil Iukhtanov

Title: AFT-tracks is a tool to analyze the interplay between cell migration and the extracellular matrix

Supervisor(s): Guillaume Jacquemet

Number of pages: 70 pages

Date: 6.5.2026

Abstract

Cell migration underlies key processes in living organisms, such as morphogenesis, immune response, wound repair, and tissue homeostasis. In different processes, cells can use various migration modes that define the mechanism of cell migration. Despite the variability of migration mechanisms, analysis of migration behavior is based on quantitative migration metrics. Calculation of these metrics relies on specialized tools that can reveal the cell migration features, such as velocity, directionality, and displacement. In addition to the cell migration behavior description, another crucial factor regulating cell migration is the ECM. ECM acts as the substrate that migrating cells follow and interact with. Importantly, physical parameters such as ECM orientation and morphology directly affect cell migration behavior. Despite this clear connection between cell migration and ECM features, there is a lack of an open-source tool to reveal the interplay between ECM properties and migrating cells. Here, we introduce the open-source AFT-tracks tool, which combines cell track analysis with assessment of ECM orientation and morphology. Cell track feature calculations are integrated with CellTracksCollab, while ECM orientation is determined using the Alignment by Fourier Transform (AFT) tool. The ECM morphology is calculated using the Multiscale Ridge-Detection algorithm, which provides structural features describing ECM complexity, density, porosity, and branching. In AFT-tracks, we propose AFT-AI metrics that define a coefficient of alignment between tracks and ECM orientation. We present AFT-tracks as a user-friendly, open-source tool for studying the interplay between migrating cells and ECM, enabling new insights into these interactions.

Keywords: cell migration, extracellular matrix (ECM), alignment, extracellular matrix structure

List of Abbreviations

AFT – Alignment by Fourier Transform

CI – Chemotaxis Index

CTC – Cell Tracking Challenge

ECM – extracellular matrix

FFT – Fast Fourier Transformation

FMI – Forward Migration Index

MSD – Mean Squared Displacement

RD – Ridge-detector

SI – Straightness Index

TAD – Turning Angle Distribution

Table of contents

1 Introduction

1.1 Literature overview

1.1.1 Cell-environment interaction as a key modulator of biological processes

Cell migration underlies key processes in living organisms, such as morphogenesis, immune response, wound repair, and tissue homeostasis (Cheng and Zygourakis, 2012). Cell motility is present in most living organisms in collective and single-cell migration forms (Lintz et al., 2017a). In this section, I focus on single-cell migration modes and the role of cell-environment interactions in cell motility.

Role of cell migration in living organisms

Cells can use various modes to migrate, including actin polymerization- and adhesion-based mechanisms, amoeboid bleb-based cell motility, and movement using an osmotic engine (Alonso-Matilla et al., 2025). The actin polymerization- and adhesion-based mechanism is described by Alonso-Matilla et. al. (2025) as “The standard mode of cell migration”. It involves actin polymerization to form protrusions of the plasma membrane, which serve as sites for the assembly of adhesion machinery. The amoeboid bleb-based cell motility is actively used in embryonic, cancer, and immune cells. This mode involves the actin-myosin network generating pressure as protrusions called blebs. Initially, newly formed protrusions lack actin network; however, as protrusions develop, a new actin-myosin network forms beneath the bleb membrane sequentially, pushing the cell border outward (Schick and Raz, 2022). The osmotic engine mode uses the osmotic pressure gradient in cell motility, which can be observed, for example, in cancer cell migration (Morishita et al., 2019). It involves local water flux and ion transport to generate forces for cellular movement.

However, despite the presence of above-described mechanisms, there is no strict, unambiguous division of cell migration modes, and authors have defined them differently. For example, some authors split migration modes into amoeboid and mesenchymal, which are characterized by different cell morphology and behaviour (Lintz et al., 2017b; Liu et al., 2015). In addition, there is still an open question: can every

single cell have all types of cell migration modes, and how many modes exist (Mierke, 2020)?

This uncertainty in the definition of cell migration modes does not change the fact that cells can adapt their migration behaviour throughout the lifespan. Thus, cell migration modes can be adapted to various functional cases. For example, leucocytes use an amoeboid mode of migration, which allows them to rapidly scan the environment and process signals (Friedl and Weigelin, 2008). Despite adaptations in cell migration behaviour throughout the lifespan, the drivers of these changes remain unclear. However, it is a fact that cell-environment interactions modulate cellular motility, which will be discussed in the following part.

Extracellular matrix role in cellular migration

Predominantly, cells interact with the extracellular environment through cell-substrate adhesions. Notably, the primary mechanism for cell migration on 2D surfaces is through cell adhesions. However, in 3D confinement, cells can also migrate without relying on adhesion to the surrounding volume environment (Paluch et al., 2016). The primary substrates for cellular adhesion in living organisms are neighbouring cells and the extracellular matrix (ECM) - a complex network composed of collagens, proteoglycans/glycosaminoglycans, elastin, fibronectin, laminins, glycoproteins, and non-fibrillar proteins, which collectively provide the structural foundation for cells (Naba, 2024; Theocharis et al., 2016). Synthesis of ECM components is regulated by cells, which define the physical, mechanical, and chemical properties of ECM in the surrounding environment (Pally and Naba, 2024a).

The production of ECM proteins depends on the matrisome - a list of genes that are responsible for the composition of the ECM. The list of human core ECM proteins includes 277 genes, of which 44 encode collagens, 36 encode proteoglycans, and 197 encode ECM glycoproteins (Naba, 2024). Also, the matrisome is dynamic and expression of genes varies among different tissue types. For example, the composition and proteomics of normal tissue and the tumor niche differ, which affect cancer development and metastasis (Socovich and Naba, 2019).

The ECM properties and cell migration are closely interconnected (Yamada and Sixt, 2019). Moreover, cell-ECM communication is bidirectional: ECM can affect cell migration through its mechanical properties and signaling molecules, and cells can alter the ECM's structure (Pally and Naba, 2024a). Example of the ECM influences cell migration through amoeboid leucocyte migration and polarization, which rely on ECM degradation products, including collagen, fibronectin, and elastin fragments (Friedl and Weigelin, 2008). Example of cell migration influences ECM proteolytic activity in primary tumor cells, changing the ECM structure during cancer cell invasion (Stetler-Stevenson and Yu, 2001).

Cancer cell invasion is also a good example of how the ECM state affects cell migration modes. Thus, tumour cells spread in different ways: as individual cells via the mesenchymal mode, which is controlled by cytoskeletal contractility and integrin-mediated ECM adhesion, or through amoeboid modes, in which they squeeze through narrow spaces of the ECM via proteolysis-independent ECM remodelling (Pourjafar and Tiwari, 2024). Investigation of the interrelationship between ECM and cell migration requires specific assays (Crossley et al., 2024a), which are described in the following section.

1.1.2 How to study cell migration and ECM interaction?

To study the interplay between cells and their surroundings, researchers commonly use migration assays that involves the cell interactions with the ECM components. However, cell migration behaviour is commonly considered independently of the ECM's structural, chemical, physical, and mechanical properties (Pally and Naba, 2024b).

The chemical properties of the ECM are determined by its molecular composition and can be studied through matrisome characterization using bioinformatics methods, immunostaining, mass spectrometry, and specialized high-throughput techniques for the analysis of specific molecular components, such as glycosaminoglycans and proteoglycans (Crossley et al., 2024b). The physical and mechanical properties include structural parameters of the ECM: crosslinking, stiffness, confinement, topography, fiber alignment, and elasticity (**Fig. 1**) (Vasudevan et al., 2023). These parameters can be estimated using various microscopy techniques, such as atomic force, traction force,

and nanonet force microscopy. Also, properties of the ECM can be revealed using a combination of fluorescent dyes, sensitive to ECM components, and optical microscopy techniques (Poole and Mostaço-guidolin, 2021).

Figure 1. Structural characteristics of ECM (fiber-like structures). All the presented ECM properties reflect on cell-ECM interplay. Illustration adapted from Yamada et al., 2022.

To understand the interplay between cell migration and the environment, the simplest approach is to use 2D cell migration assays, such as wound-healing and transwell migration assays. The first describes the ability of cells to close artificially introduced scratches, while the second estimates the ability of cells to invade in the presence of a chemoattractive cue (Justus et al., 2014). However, 2D assays have limited ability to reflect the cell-ECM interaction in the *in vivo* environment, necessitating the use of 3D models (Habanjar et al., 2021).

To obtain the 3D-native ECM in its *in vivo* state, the ECM can be directly isolated from organs via decellularization. Despite decellularization modulating the *in vivo* state of the matrix, this method lacks tunability, is limited in reproducibility, and may elicit toxic responses due to decellularization agents. Thus, other popular methods that provide tunability and reproducibility for ECM modulation *in vitro* are synthetic and hybrid hydrogels, spheroids, and cell-derived matrix models. The synthetic and hybrid hydrogels are highly hydrated 3D polymeric scaffolds composed of physically or chemically cross-linked ECM-derived proteins, including collagen derivatives, glycoproteins, polysaccharides (Morales et al., 2021). The widely applied methods for modulating volume cell-ECM communication are spheroid- and CDM-based assays. The spheroids are cell suspensions in plates that closely approximate the living cell environment (Vinci et al., 2015). The CDM assay uses cell lines to make the matrices on which cells are cultured (Kaukonen et al., 2017). This method offers a more *in vivo*-relevant model than models using purified matrix proteins. Additionally, most synthetically or hybrid-generated ECM models can be modulated. For example, the orientation and alignment of ECM components can be altered via electrospinning (Padhi and Nain, 2020).

All of these cell-ECM modulations are actively applied in practice, for example, to the investigation of tumour cell migration behaviour dependence on ECM alignment (Ray et al., 2017), the effect of various matrix connectivity on macrophages and fibroblasts migration (Ford et al., 2019; Slater et al., 2021), the effect of ECM topography on cellular migration (Park et al., 2016), and effect of fiber density and ECM stiffness on cell migration modes (Hiraki et al., 2023). In each of the listed examples, cell features such as directionality and total displacement are pivotal for interpreting the effects of ECM properties on cellular migration behaviour. In the following section, I will describe the cell migration metrics that are commonly used in cell migration assays.

1.1.3 Cell migration metrics

Cell migration metrics are a common way to describe cell migration behaviour in experimental setups. Importantly, the assays also define metrics useful for describing cell migration in specific conditions. Thus, there are common metrics for cell migration

assays, as well as specific metrics for some assays, e.g., the wound closure metric for the wound healing assay (Varankar and Bapat, 2018). In this section, I will describe the assay-unspecific metrics and their application in cell migration analysis (**Table 1**).

Table 1. The main cell migration metrics.

Metric group	Formulas
Cell speed and velocity	$v_{x,n} = \frac{r_{x,n}(t_{i+1}) - r_{x,n}(t_i)}{\tau}$; $v_{y,n} = \frac{r_{y,n}(t_{i+1}) - r_{y,n}(t_i)}{\tau}$ $r_{x,n}(t_i)$ - *position of cell n along the x-axis at time point* t_i $r_{y,n}(t_i)$- *position of cell n along the y-axis at time point* t_i τ - *time interval between two consecutive frames* $(t_{i+1} - t_i)$
Displacement	$dR(t,\tau) = \big(dx(t,\tau), dy(t,\tau)\big)$ $d_{euclidean} = \sqrt{(x(t_{i+1}) - x(t_i))^2 + (y(t_{i+1}) - y(t_i))^2}$ $d_{net} = \sqrt{(x(t_0) - x(t_{max}))^2 + (y(t_0) - y(t_{max}))^2}$ $MSD = \langle (x(t+\tau) - x(\tau)^2 + y(t+\tau) - y(\tau)^2) \rangle$
Directionality and Persistence	$CI = \frac{d_{directional}}{d_{total}}$; *d - distance* $FMI_{x\ or\ y} = \frac{\Delta x\ or\ \Delta y}{d_{total}}$
Angular and Path	$SI = \frac{d_{net}}{d_{total}}$ $\theta_i = cos^{-1}\left(\frac{\Delta r_i \times \Delta r_{i+1}}{\lvert\Delta r_i\rvert \times \lvert\Delta r_{i+1}\rvert}\right)$; $TAD = \langle \sum \theta_i \rangle$ Δr_i- *displacement vector for migration step i* Δr_i- *magnitude (length) of displacement vector* $\Delta \boldsymbol{r}_i$

Cell Speed and Velocity

Cell migration speed and velocity are used to represent cell behaviour over the time. It can be measured as instantaneous speed, which depends on the specific interval between two neighbouring time points, or overall average pathway speed. The velocity

metric is the same as speed, but it includes direction. A good example of the application of the cell speed metric in biological studies is the investigation of the ECM's effect on cell migration. Thus, cell speed can reflect proteolytic and nonproteolytic activity during migration on the ECM (Ehrbar et al., 2011).

Displacement metrics: Accumulated distance, Euclidean distance, and MSD

The displacement metrics represent the distance cells travelled during time. The accumulated distance quantifies the total length of the cell path, while Euclidean distance calculates the distance from the start to the end point. The Euclidean distance goes hand in hand with Mean Squared Displacement, a metric that is the square of the Euclidean distance. Essentially, it is a box covering the area of cell displacement between the start and finish points, indicating cell migration behaviour: directed, random, or confined. A good illustration of independence and the importance of all displacement metrics is research that compares vascular smooth muscle cell migration across varying stiffness and ECM protein-coated hydrogels. Thus, different displacement metrics capture different aspects of cell migration. On Fibronectin (FN), both migration distance and MSD increased with substrate stiffness, indicating enhanced motility. In contrast, on Collagen-1 (COL1), migration distance decreased with stiffness, while MSD was highest on the stiffest substrate, suggesting slower but more persistent directional migration (Rickel et al., 2020).

Directionality and Persistence metrics: Chemotactic Index (CI) or Forward Migration Index (FMI)

The directionality and persistence metrics indicate the cells' tendency to move in one direction. The chemotactic Index (CI) quantifies how directed a cell migration is relative to the gradient, while the Forward Migration Index (FMI) defines the part of the distance travelled in each of the four directions: up, right, down, and left. The CI and FMI are close to each other and can be useful in experiments with chemical (Vasaturo et al., 2012) or mechanical (Hartman et al., 2017) gradients in the extracellular environment.

Angular and Path metrics: Turning angle distribution (TAD), Straightness index (SI)

The angular and path metrics represent the trajectory of the cell migration. The turning angle distribution (TAD) quantifies the angles between sequential movement steps, either globally or locally. The global TAD describes the angle of the current direction relative to a fixed coordinate axis, while the relative TAD describes the angle of a path segment relative to the previous segment, providing insights into local persistence and movement dynamics.

The straightness index (SI) quantifies how straight the cell was during the path. Both TAD and SI metrics are sensitive to changes in environmental structure and are therefore widely used to characterize persistence and directionally biased cell migration. For example, in cell migration within collagen hydrogels, fiber alignment significantly alters both TAD and SI. In aligned collagen matrices, the TAD shows smaller angles and less variability, thereby increasing directional persistence along the fiber orientation. In contrast, cells migrating in unaligned matrices have broader TAD, indicating more stochastic, undirected movement (Pruitt et al., 2020).

Metrics limitations

Description of cell migration through the specific metrics has limitations and requires careful selection for analysis. The limitations of speed and velocity metrics stem from sample size and track length. Thus, small tracked populations are often unrepresentative and noisy. Also, the instantaneous velocity can be unrepresentative if the cell moved back and forth in the gap between time-point imaging.

The limitations of displacement metrics include the frequency of imaging and the averaging of cell populations or time points for a single cell. For example, it affects the MSD metric: the cell population is heterogeneous, and each cell behaves differently; as such, a cell can migrate differently over time based on extracellular conditions, such as changes in ECM properties in the local environment, along the path between two time points. The directionality, angular, and path metrics have a limitation in terms of time duration. Thus, CI cannot be estimated if cells have a small number of time points. In contrast, SI will be close to zero if the cell pathway is too long.

To bypass these limits, authors apply different methods. One method to overcome the time-point limitation is to use a rolling window. The rolling method computes an average over a set of time points specified by the user. Thus, for example, the estimation of SI for long tracks is less likely to shift to zero than under the classic approach. The other approach is to modify the metrics by using corrected metrics. Thus, to exclude the trend to SI going to zero, apply the corrected SI, which includes the square root of the duration-multiplication term from the classical SI approach (Beltman et al., 2009).

In addition to the limitations of cell migration metrics, segmentation inaccuracies and tracking mistakes can affect the results of further cell migration data analysis (Wiggins et al., 2025). In the next section, I will discuss approaches to segmenting and tracking cell migration data.

1.1.4 Tools for cell migration data analysis

The extraction of cellular migration metrics begins with the segmentation of migrating cells -the process of defining object regions and separating them from the background. The segmentation time, method, and accuracy depend on the imaging technique used to collect the data. Migrating cells can be imaged with fluorescent (labelled) or brightfield (label-free) approaches. The first one is associated with phototoxicity and invasion in the native cell state, while the second is associated with low phototoxicity and minimal invasion (Ghosh and Agarwal, 2023). Labelled cells segmentation is commonly based on fluorescent tags, whereas label-free segmentation faces difficulties due to smooth cell borders and limited contrast with the background.

The segmentation of the cells can be done manually or automatically with the option to further manual correction (Vicar et al., 2019). Manual segmentation involves visual detection of cell borders and labelling each cell, which is a time-consuming process (Vădineanu et al., 2024). The manual labelling can be performed through the platforms that include manual labelling functionality, such as Fiji (Schindelin et al., 2012). Automatic or semi-automatic segmentation requires training the model for cell segmentation or using prepared models. One tool used to achieve this goal is Cellpose (Stringer et al., 2020). Cellpose includes several U-Net-based architectures that can be applied to various cell imaging datasets. The segmentation output can contain two

labels background and cells (semantic segmentation), or several labels with background and individual value for each cell (instance segmentation) (**Fig. 2**). The output mask can also be corrected manually or using an object-separation algorithm (e.g., a watershed algorithm). Various automatic detection tools exhibit different accuracy across datasets, indicating that model selection should be specified for specific dataset and goal (Liu et al., 2024).

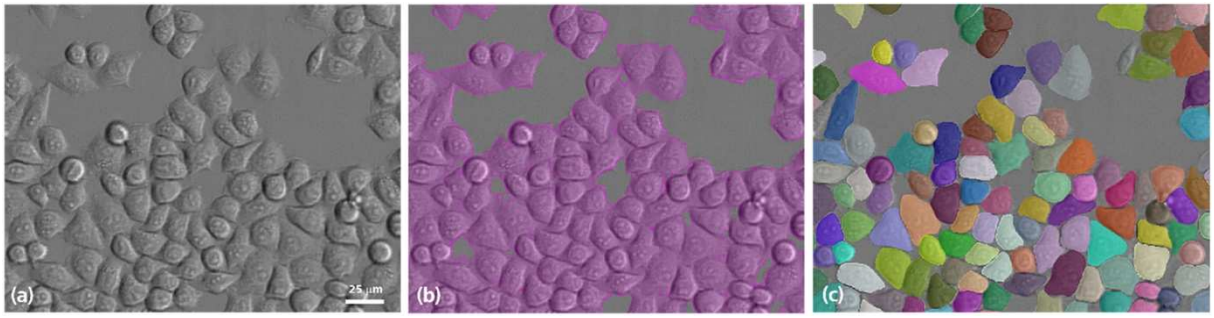

Figure 2. The example of *s*emantic (b) and instance (c) segmentation of cell migration data (a). Semantic segmentation contains cells (purple color) and background (gray), whereas instance segmentation assigns an individual label to each cell and 0 to the background. Illustration adapted from Bhattiprolu, 2025.

The segmentation step is followed by the tracking step, which detects changes in cell location over time. It can be performed manually, semi-automatically, or fully automatically (Meijering et al., 2012). The algorithm can be broadly divided into two categories: tracking by contour evolution methods and tracking by detection methods (Ulman et al., 2017). The contour evolution approach simultaneously solves the segmentation and tracking goals, as it defines the cell contour in the first frame and later tracks changes in the cell border. The detection approach is based on preliminary segmentation of cells with the following generation of “tracklets” - variables that link a detected candidate in one frame with a candidate in the following or previous frames. The automatic linkage of cells on different frames faced problems, including cell mitosis, apoptosis/exit, appearance/entry, and touching/clustering (Yazdi and Khotanlou, 2024). These events increase the dynamics and decrease the predictability of detection, introducing ambiguity into cell association, which is handled differently in various software.

Tools for cell tracking analysis can be commercial and open source; a comprehensive list is provided in Emami et al., 2021. Both types of tools combine manual and automatic tracking methods. For example, TrackMate v.7 (Ershov et al., 2022) provides manual tracking and automated detection based on deep learning methods for object segmentation. Comparing algorithms can be done by applying them to open-cell migration databases, such as the Cell Tracking Challenge (CTC) (Ulman et al., 2017). Various algorithms show different accuracies in cell tracking across real-time imaging datasets from the CTC. The development of open-science platforms for cell migration analysis increases reproducibility, transparency, and standardized benchmarking of tracking algorithms across different datasets and experimental conditions.

Despite the wide range of tools, all of them provide the tracks' coordinates along with a bunch of cell migration metrics as output. However, the majority of tools analyse only cell migration behaviour, without linking it to the estimation of environmental conditions, such as the ECM structural parameter. In the next section, I will describe tools for extracting ECM features.

1.1.5 Tools for ECM imaging analysis

The mechanical, physical, and chemical properties of ECM are interconnected. To describe ECM, researchers commonly use microscopy imaging. I will focus mostly on tools that extract structural features from brightfield and fluorescent ECM imaging.

Tools for ECM feature extraction based on various algorithms, but all of them execute quantitative metrics, including fiber orientation, fiber alignment, fractal dimension, pore size/porosity, fiber diameter, fiber length, fiber density, and number of branches and endpoints (**Fig. 3**). Some of these tools are designed specifically to describe ECM data, while others were initially developed for detecting fiber-like structures on the images. For example, some tools initially developed to detect the vascular net, but also can be successfully used for ECM components detection, such as fibrin (de Vries et al., 2023).

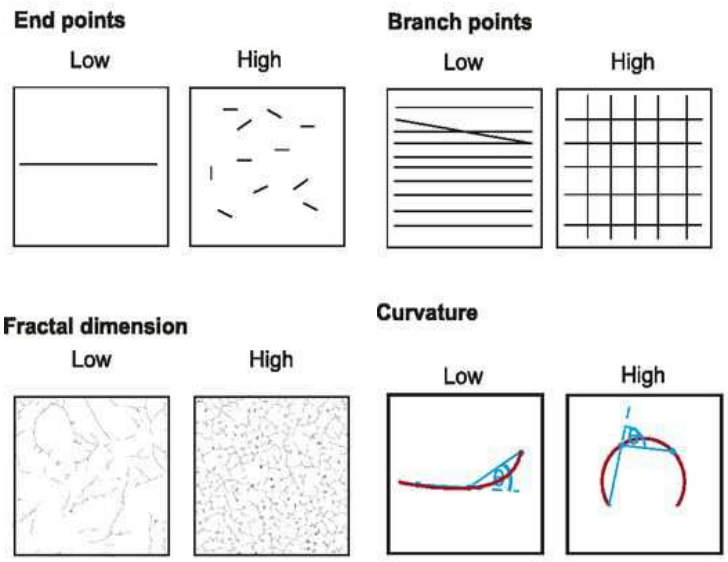

Figure 3. Example of metrics to estimate ECM structure. Black lines represent the ECM fibers. The endpoints and branchpoints are classified as network points; the fractal dimension describes the complexity of the net; the curvature describes the straightness of the fibers. Illustration adapted from Wershof et al., 2021.

The algorithm for ECM alignment extraction can be grouped into three categories: intensity-derivative/structure-tensor algorithms, Fourier- and spectral-based algorithms, and directional-filter/transform algorithms. The intensity derivatives and structure vectors process pixel intensity changes in an area called the structure tensor for each pixel, evaluating local predominant orientation, energy, and coherency; examples of tools implementing this approach include OrientationJ (Püspöki et al., 2016) and FibrilTool (Boudaoud et al., 2014) plugins. Spectral analysis and the Fourier transform method decompose the image into periodic components, which are analyzed more quickly than with other approaches; examples of tools implementing this approach include FiberFit (Morrill et al., 2016), CytoSpectre (Kartasalo et al., 2015), and Alignment by Fourier Transformation (AFT) (Marcotti et al., 2021). The directional-filter/transform algorithms use specific filters, such as the curvelet filter, to analyze orientations in images; examples of tools implementing this approach include CurveAlign (Liu et al., 2017) and CT-FIRE (Bredfeldt et al., 2014).

Besides alignment, the remaining structural parameters can be based on the initial segmentation result of the fiber network or directly derived from images. Also, some of

them can extract almost all structural characteristics of the ECM. For example, TWOMBLI (Wershof et al., 2021) uses an initial multiscale Ridge-Detector (RD) segmentation followed by a comprehensive description of the ECM structure with various plugins. The other tools can extract only a few ECM metrics. For instance, DiameterJ (Hotaling et al., 2015) can obtain diameter description, universal porosity, pore areas, and branch points.

Tools for analyzing ECM connectivity and topology commonly rely on skeletonization or graph theory and are implemented, for example, in StructuralGT (Vecchio et al., 2021) and DiameterJ softwares. The fiber density is usually defined as the area occupied by fibers divided by the image area, implemented in AngioTool (Zudaire et al., 2011), REAVER (Corliss et al., 2020), or ACCMetrics (Chen et al., 2017).

Along with various tools, some authors use custom code to extract ECM parameters and quantify cell migration (Wang et al., 2018). This indicates a lack of open-source and standardized tools to describe cell-ECM dependence, and there is a need for an open platform that can reveal the interconnection between ECM parameters and migrating cells.

1.2 Aims and hypotheses

Therefore, the aim of my study is to develop an open-source, user-friendly AFT-tracks tool for analysing the dependence of cell migration behaviour on the ECM. To achieve the aim of this project, we set the following goals:

1. Develop new metrics to quantify the relationship between cell migration tracks and the ECM.

2. Validate new metrics on synthetic and experimental brightfield and fluorescent datasets.

3. Adapt usage of the tool for the Google Collab platform and local running.

AI note: Grammarly was used for checking grammar mistakes; text was not restructured or rewritten by AI. ChatGPT was used for the translation of some words and collocations.

This type of prompt was used: “Can you translate <word or collocations in my native language> in English, give me options in academic writing style?”. ChatGPT is also used for coding: bug fixation, code generation, and code restructuring. I also worked with NotebookLM from Google and asked questions based on the articles’ material.

2 Materials and methods

2.1 Overview of AFT-tracks workflow

The aim of the AFT-tracks tool is to combine cell migration and ECM features extraction to find dependencies between them. To estimate the ECM properties, AFT-tracks uses two approaches: FFT- and segmentation-based. The first approach is a direct implementation of the Alignment by Fourier Transformation tool (AFT); the pipeline was precisely described in the original work (Marcotti et al., 2021). The AFT applies the Fourier Transformation Algorithm to extract the orientation of the ECM. The second approach was inspired by the Fiji plugin called TWOMBLI (Wershof et al., 2021) and implemented the multiscale Hessian Ridge-detector to segment the ECM structure. To estimate cell migration behavior, AFT-tracks used CellTracksColab (Gómez-De-Mariscal et al., 2024) functionality and provided extended spot-level metrics. The AFT-tracks can handle single and multi-frame .tiff image formats and the .csv spots file format as input. Both image and spots' data can be downloaded through Google Drive. The main AFT-tracks pipeline presented in **Fig. 4**.

The AFT-tracks pipeline was implemented in Python language using computational NumPy, SciPy, pandas libraries, and additional packages for specific image processing algorithms, such as scikit-image, OpenCV, matplotlib, seaborn, skan, ridge-detector. Also, AFT-tracks follow the Jupiter Notebook structure that can combine code, text, and visualization in one document with step-by-step interactive organization (Kluyver et al., 2016). The organization of the code in separate cells also gives flexibility in choosing suitable methods for specific experiments. The installation procedure and the latest version of instructions are available on the AFT-tracks GitHub page (https://github.com/CellMigrationLab/AFT_tracks).

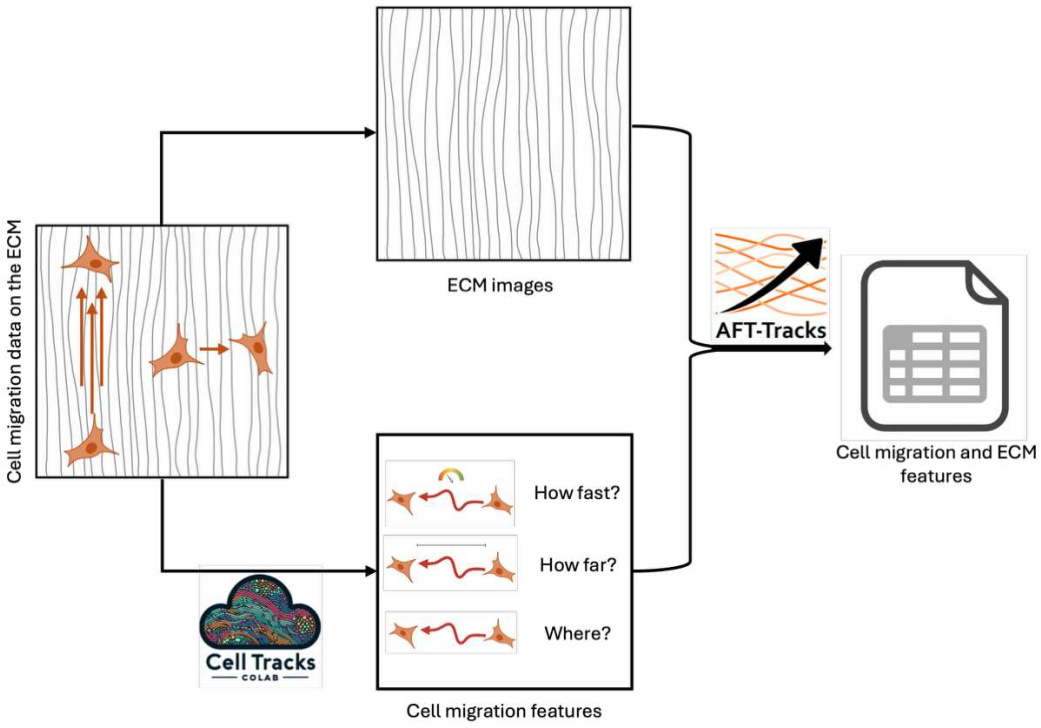

Figure 4. Schematic illustration of the AFT-tracks pipeline. The AFT-tracks take as an input cell migration data on the ECM and give an output table with cell migration and ECM features.

2.2 Local patch integration of the ECM and cell migration

Recent research has shown that the local structure of the ECM affects cell migration behavior (Carey et al., 2016; Zhao et al., 2025). To extract ECM local features, the AFT-tracks implemented description of ECM and cell migration on local patch level (**Fig. 5**). The whole image was split into several equal size patches using predefined parameters that describe area size and overlap between patches. Patch size and overlap between patches were defined by the variables ‘windows_size’ and ‘overlap’. Patches can be filtered based on intensity thresholds, eccentricity thresholds, or mask filtering, which are defined by user-defined variables ‘intensity_thresh’, ‘eccentricity_thresh’, and ‘mask’, respectively.

Following the patch splitting, each patch received a unique ID. Patch central coordinates were used to affiliate migrating cells with the closest patch using the KDTree method. The final cell migration features were calculated as mean values of segments (if the segment-based approach was used) or spots (if the rolling window

approach was used) within the patch. The output results of the alignment analysis can additionally be exported as figures of tracks and ECM orientation in each patch and cell migrating spot.

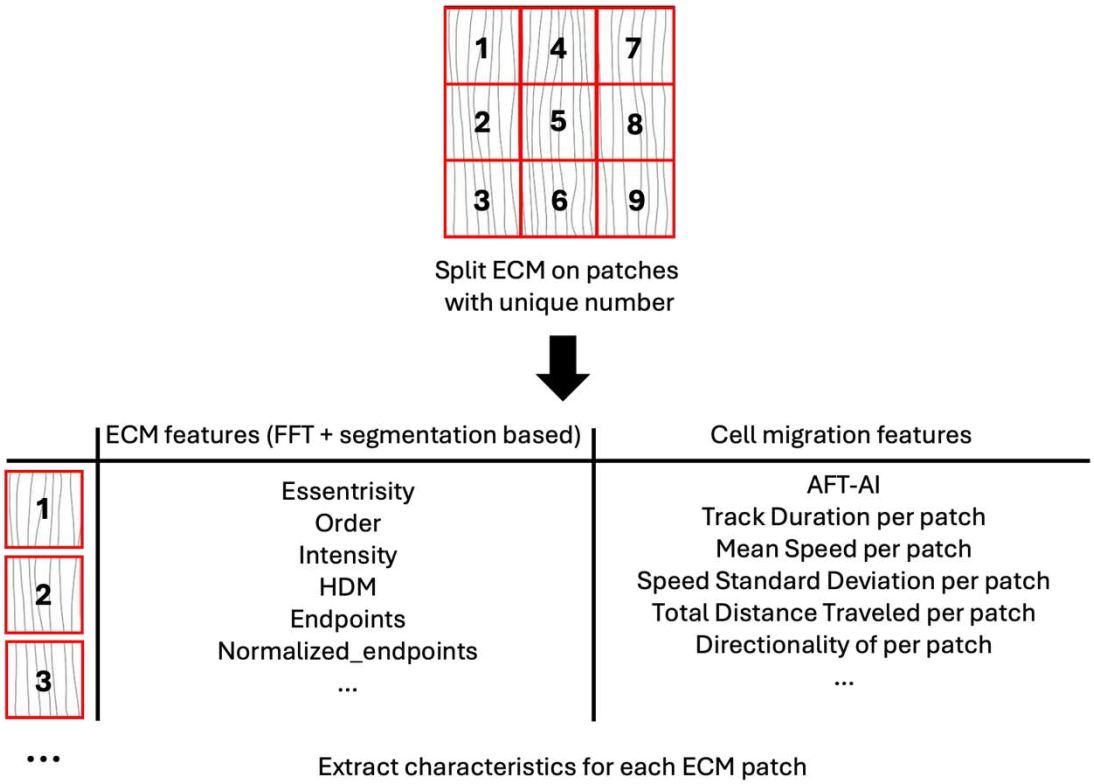

Figure 5. Patch-level approach to features extraction. The AFT-tracks took small patches and calculated cell migration and ECM metrics locally. Red boxes represent patch borders, numbers respresent patch_ID.

2.3 ECM properties quantification

2.3.1 FFT-based approach

The Fast Fourier Transform (FFT) is one of the most widely used tools for transforming images into the frequency domain, enabling rapid feature extraction without the need for complex preprocessing. In AFT-tracks, the FFT-based approach provided information about orientation, eccentricity, and order metrics of the ECM (**Fig. 6**). This approach repeated the functional part of the AFT, except for order metrics. AFT-tracks calculate the order parameter for each patch, specifically, which varies from the original AFT approach, where the order parameter is defined for the whole image.

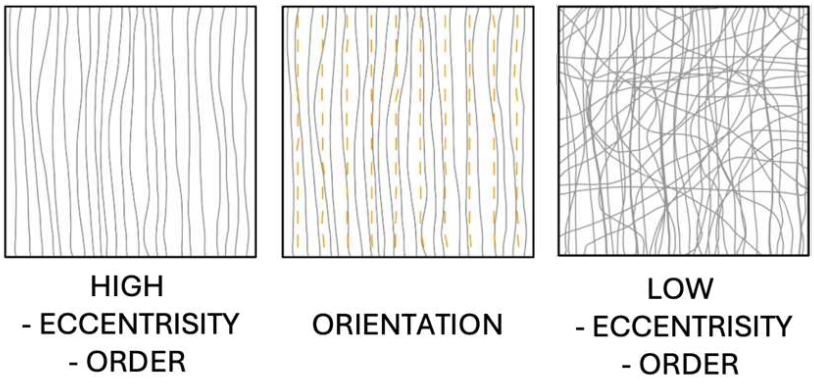

.

Figure 6. The FFT-based metrics of the ECM state. The left image shows an ECM with a *single* dominant fiber orientation (high eccentricity) and the same alignment across neighbouring local patches (high order). The middle image shows the orientation detected in each ECM patch.

Local order calculation in the AFT-tracks was defined by the function 'AFT_order_parameter'. The 'AFT_order_parameter' took the mean difference between the orientation angle of each selected and neighbouring patches. The neighbor patch number was controlled by the user-defined variable 'neighborhood_radius'. Higher-order values indicate strong local fiber alignment. Thus, the value 1 means strong alignment with local neighbours, while 0 means that the patch is not aligned with local neighbors.

2.3.2 Segmentation-based approach

Settings and contrast enhancement

Despite the fast and easy implementation of the FFT approach, it is not applicable for the segmentation of the ECM to estimate morphology. The structural features of ECM represent physical, mechanical, and chemical features. In AFT-tracks, the segmentation-based approach provided information about the ECM pattern structure (overall pipeline in **Fig. 7**). This method was based on the multiscale Hessian Ridge-detector that was implemented by a manually written pipeline, whose functions are located in the file segmentation.py. The initial step of the segmentation is deferment of input parameters:

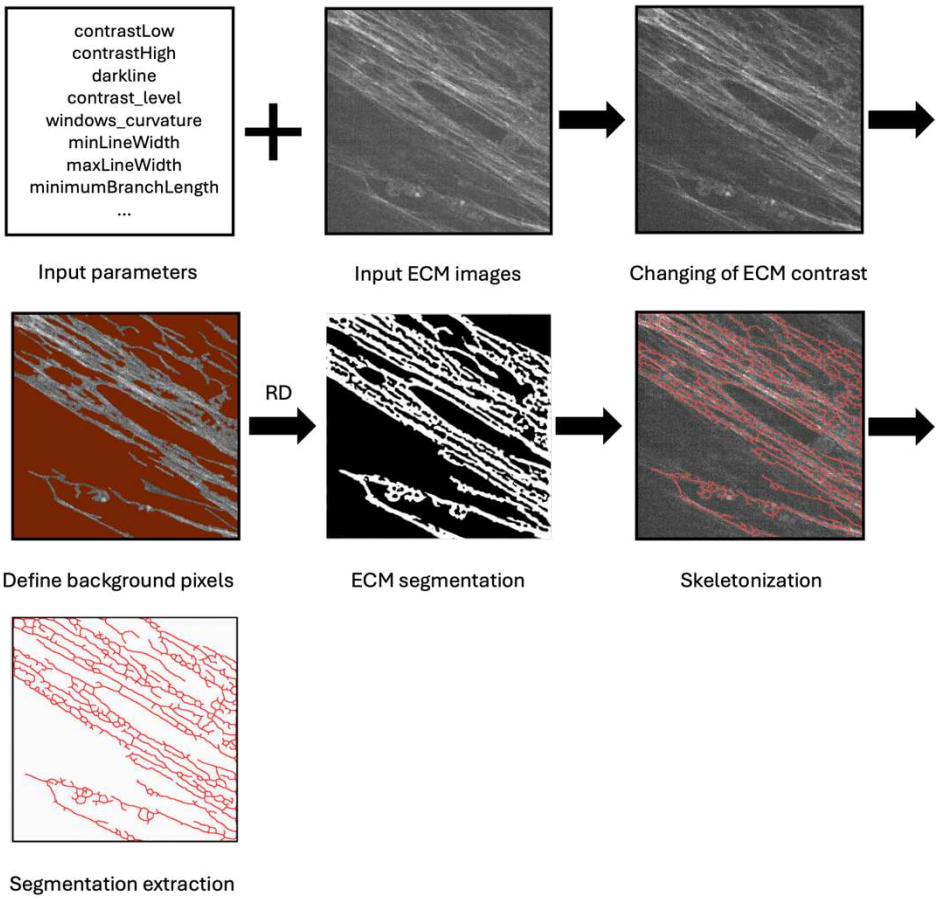

Figure 7. The segmentation-based approach pipeline. The pipeline takes ECM images and user-defined parameters as input. The processing steps include contrast enhancement, background removal, segmentation, and skeletonization of the resulting mask, followed by feature extraction. RD - multiscale Hessian ridge detector.

1. 'contrastLow'/'contrastHigh' – the intensity-based threshold levels for the Ridge detector; vary from 0 to 255;

2. 'intensity_clip_percent' – the percent of pixels that are clipped from the image to enhance contrast; varies from 0 to 100;

3. 'darkline' – the boolean parameter that defines the color of the ECM components relative to the background;

4. 'windows_curvature' – the size of the sliding window in curvature calculation; 'minLineWidth'/'maxLineWidth' – the range of line width that is detected in the multiscale Ridge detector;

5. 'do_skeleton' – the boolean parameter that defines skeletonization of the Ridge detector output mask to extract ECM morphology features;

6. 'prune_short' – the boolean parameter that defines the exclusion of short branches after skeletonization;

7. ' minimumBranchLength ' – the minimum branch length threshold (in pixels) used to filter skeleton branches

The following step is changing the contrast that was defined by the function 'enhance_contrast', in which the intensity distribution of images was clipped by the percent defined in 'intensity_clip_percent', and subsequently normalized to the range [0, 1].

Multiscale Ridge detection

The multiscale Ridge detection algorithm uses to detect ECM ridge-like components on the images(Shokouh et al., 2021). In the initial step, the sigma and threshold values were defined by functions calcSigma, calcLowerThresh, and calcUpperThresh, adapted from TWOMBLI tool. The σ size in the Gaussian filter was calculated as $\sigma(w) = \frac{w}{2\sqrt{3}} + 0.5$, where w is line width. The lower threshold (T_{low}) was calculated as:

$$0.17 \times \left| \frac{-2 \times (C_{low}) \times (w/2)}{(\sqrt{2 \times \pi} \times \sigma^3)} \times e^{-(w/2)^2 / 2 \times \sigma^2} \right|, \; C_{low} = \begin{cases} contrastLow, \; if \; darkline = False \\ 255 - contrastHigh, \; if \; darline = True \end{cases}$$

The high threshold (T_{high}) is calculated as:

$$0.17 \times \left| \frac{-2 \times (C_{high}) \times (w/2)}{(\sqrt{2 \times \pi} \times \sigma^3)} \times e^{-(w/2)^2 / 2 \times \sigma^2} \right|, \; C_{high} = \begin{cases} contrastHigh, \; if \; darkline = False \\ 255 - contrastLow, \; if \; darline = True \end{cases}$$

After that, multiscale Ridge-detection was applied to the image with enhanced contrast. For each range of line width, the image was convolved with a Gaussian kernel defined by the 'calcSigma' function. To each pixel of the convolved image, the Hessian matrix calculation was applied, with the following extraction of eigenvalues. The Hessian

matrix was computed as $\begin{pmatrix} I_{xx}(x,y) & I_{xy}(x,y) \\ I_{xy}(x,y) & I_{yy}(x,y) \end{pmatrix} = \begin{pmatrix} H_{11} & H_{12} \\ H_{21} & H_{22} \end{pmatrix}$. The eigenvalues were computed as $\begin{cases} k_1(x,y) = 0.5(H_{11} + H_{22}) - 0.25\sqrt{(H_{11} + H_{22})^2 + 4{H_{12}}^2} \\ k_2(x,y) = 0.5(H_{11} + H_{22}) + 0.25\sqrt{(H_{11} + H_{22})^2 + 4{H_{12}}^2} \end{cases}$

The calculation of Ridge-detector response defined by function 'hessian_ridge_response', which used functions 'hessian_matrix' and 'hessian_matrix_eigvals' from 'skimge.features' library.

After that, the absolute maximum eigenvalue was taken: $D_i = max(|k_{1,i}|, |k_{2,i}|)$ for each pair of i. The output of the Hessian ridge response matrix was defined as $R_i = \begin{cases} \max(0, -D_i), \text{if darkline} = \text{True} \\ \max(0, D_i), \text{if darkline} = \text{False} \end{cases}$. The results of hessian ridges response matrix transformed in range from 0 to 255. Then, thresholding was applied to each value in the Hessian ridge response matrix. The output of this threshold is a binary mask, where each element equal $1, \text{if } T_{low} \leq R_i \leq T_{high}$, or 0 otherwise. The Ridge-detector ran for each line width in the range ['minLineWidth', 'maxLineWidth']. As an output, the multiscale Ridge-detector gave a merged binary mask from each line width iteration.

Skeletonization and branch filtering

In the next step, the output segmentation mask was skeletonized using the package skimage.morphology, module skeletonization. After skeletonization, users could exclude small branches using the function 'remove_short_components'. The function 'remove_short_components' was based on the Skan library (Nunez-Iglesias et al., 2018). The 'Skan.summarize' module gave a summary table about the skeleton pattern, classifying branches into four types: 0 – isolated segments with two endpoints, 1 – segments with one junction and one endpoint, 2 – segments with two junction points, 3 – isolated cycle segments. Additionally, Skan provided length, start/end coordinates for each segment. The function 'remove_short_components' excluded the small segment with branch types 0, 1, and 3, and gave a filtered mask as an output.

Segmentation based features extraction

The calculation of segmentation-based feature extraction was implemented in the function ‘segmentation_features’. For each patch of the original image, the ridge-detection mask and the skeletonization mask were defined as ‘im_patch’, ‘mask_patch’, and ‘skel_mask_patch’, respectively. The ‘im_patch’ was used to calculate intensity and lacunarity features. The ‘mask_patch’ was used to calculate HDM. The ‘skel_mask_patch’ was used to calculate endpoints, branchpoints, normalized endpoints and branchpoints, FFD, and curvature (**Fig. 8**). To estimate FFD AFT-tracks import box-counting function from Fractal Dimension Estimation Tool developed by Cui and Wang, 2025. To calculate curvature, the AFT-tracks used ‘curvature’ and ‘compute_curvature_from_skeleton’ functions. The curvature was calculated using a sliding-window approach. For each skeleton segment, the coordinates of the segments and their endpoints were extracted. To each segment, curvature was defined as a ratio of the average perpendicular distance of curve pixels to the line connecting segment endpoints. Curvature was normalized by the total segment length. The output curvature gave the mean for each segment in the patch.

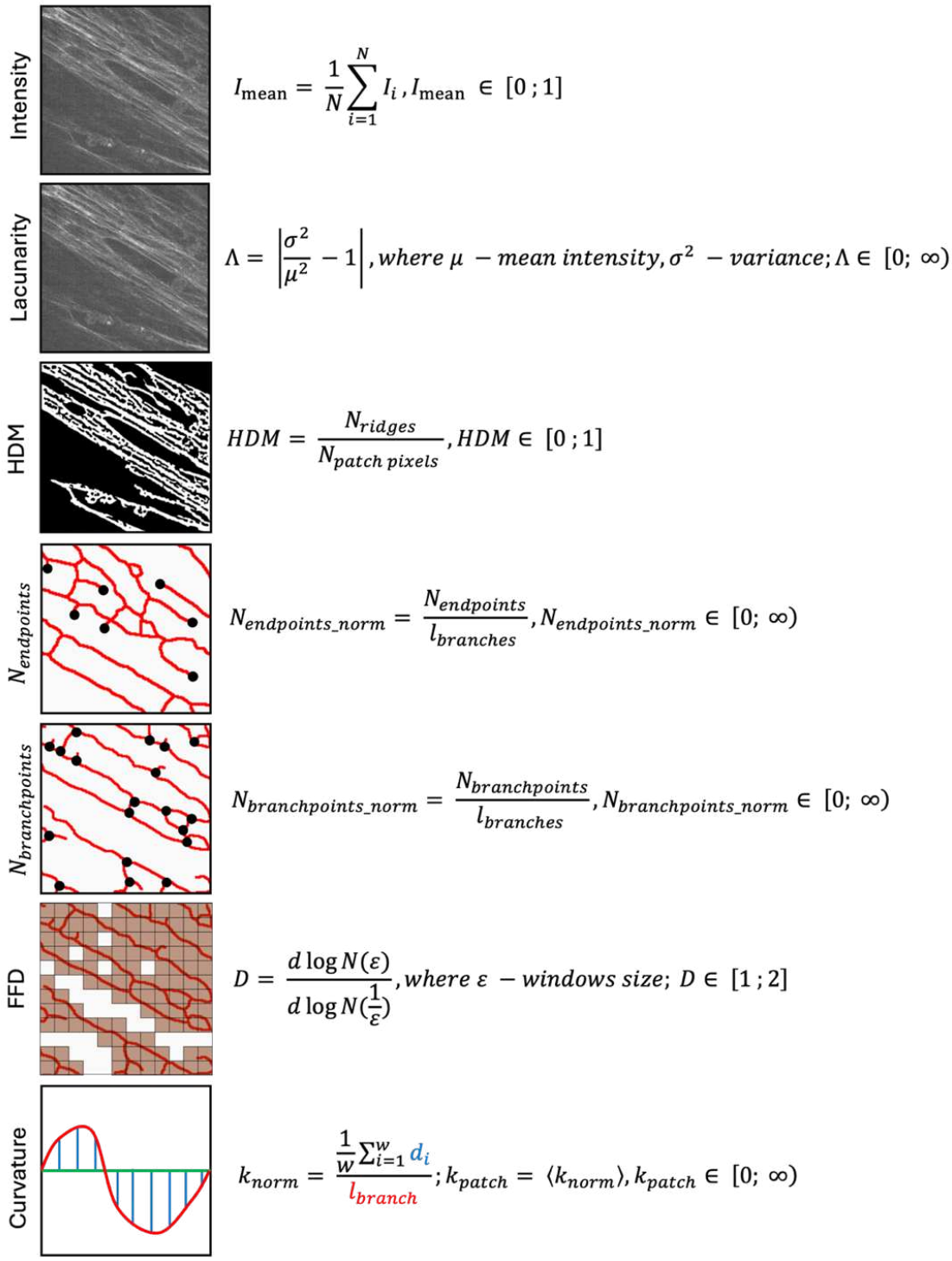

Figure 8. The segmentation-based approach metrics description. In curvature calculation d_i – perpendicular distance from the chord to the line linking the beginning and the end of the branch, w – sliding window size, l_{branch} – length of the branch.

2.4 The cell migration metrics

To quantify cell migration behavior in local patch level, AFT-tracks uses two evaluations: the mean of tracks' segments metrics in the patch or the calculation of rolling window metrics in each spot within the patch. The first evaluation was based on the existing CellTracksColab functions but applied for segments of the tracks inside the patch. The second evaluation was a repeat of the CellTracksColab functions with the 'rolling_window' calculation. Both approaches differently estimate patch local migration differently: the first of them include only tracks located in the patch, while the second one can also include data from neighboring patches. My goal was to implement and compare both.

Additionally, AFT-tracks extends the list of additional metrics with velocity correlation index (VCI): $VCI = \langle \frac{dR(t,\tau) \times dR(t+\tau,\tau)}{|dR(t,\tau)||dR(t+\tau,\tau)|} \rangle$, displacement autocorrelation function (DAF): $DAF(\tau) = \langle dx(t,\tau)dx(t+\tau,\tau) + dy(t,\tau)dy(t+\tau,\tau) \rangle$, and calculation of the Forward Migration Index metrics on the spot level: part of the spot displacement to the track length.

2.5 Datasets

2.5.1 Synthetic datasets

Synthetic datasets were created using a custom Jupiter notebook presented on the GitHub page (https://github.com/CellMigrationLab/AFT_tracks). The synthetic datasets consist of three groups of images with different fiber organization:

- High angular noise ECM ("orientation_noise_deg": 70, "noise_strength": 0.9);
- Intermediate angular noise ECM ("orientation_noise_deg": 25, "noise_strength": 0.6);
- Low angular noise ECM ("orientation_noise_deg": 5, "noise_strength": 0.4).

Common parameters for each ECM dataset: frames = 150, img_size = (512, 512), num_fibres = 500, base_orientation_deg = 90, wave_wavelength_px = 200,

wave_direction_deg = 0, phase_drift_per_frame = 0, length_range = (50, 500), thickness_range = (1, 1), center_placement = True, per_frame_anchor_jitter = 0.02, rng_seed = 42.

The synthetic datasets consist of three groups of cells with different migration behavior:

- Directionally persistent motion (jitter_deg = 20.0, bias_strength = 0.6);
- Uncorrelated random walk (common parameters);
- Persistent motion with directional reversals (reversal_prob = 0.15, reversal_hold_min = 10, reversal_hold_max = 30, reversal_target_deg = 270, reversal_jitter_deg = 20, reverse_bias_strength = 0.95).

Common parameters for each cell migration dataset: num_cells = 60, frames = 150, img_size = (512, 512), radius_px = 2, speed_range = (2.0, 4.0), seed = 7).

Synthetic cells were tracked using TrackMate using the LoG detector (estimated object diameter = 4 pixels, Quality threshold = 0.1) and the Simple LAP tracker (linking max distance = 20 pixels, gap closing distance = 40 pixels, gap-closing max frame gap = 2). Tracks that traveled less than 30 pixels were filtered out.

All combinations of ECM organization and cell migration behavior were generated, resulting in a total of nine synthetic experimental conditions. Code and generated datasets implemented by Joanna Pylvänäinen. Plots and data interpretation were done by Daniil Iukhtanov.

2.5.2 Experimental datasets

Brightfield dataset

Brightfield microscopy cell migration data on cell-derived matrixes (CDMs) were taken from a previously published study about role of L-type calcium channels in filopodia stabilization during invasion (Jacquemet et al., 2016). The one group contained untreated cells, while the other group contained Carbamazepine treated cells. The cells in both conditions were seeded on CDMs and imaged during 24 hours with 10 minutes

lag. Cells were then filmed using an inverted widefield microscope (AxioCam MRm camera, EL Plan-Neofluar 10 × /0.5 NA objective (Carl Zeiss)) equipped with a heated chamber (37 °C) and CO2 controller (5%).

The following values of parameters were used: single_frame = True; window_size = 200; overlap = 0.2; neighborhood_radius = 1; intensity_thresh = 0;
eccentricity_thresh = 0

Glioblastoma dataset

Fluorescent microscopy cell migration data on CDMs were taken from a study about the role of CCT8 in MYO10-positive filopodia formation (Popović et al., unpublished data). The one group contained control cells, while the other group contained siCCT8 cells. The cells in both conditions were seeded on CDMs for 4 hours before imaging. The imaging was done with 10 minutes lag between frames. The confocal microscope used was a laser scanning confocal microscope (LSM880, Zeiss), equipped with an Airyscan detector (Carl Zeiss) and a 40× water (NA 1.2) or 63× oil (NA 1.4) objective. The microscope was controlled using Zen Black (2.3), and the Airyscan was used in standard superresolution mode.

The following values of parameters were used: single_frame = True; window_size = 300; overlap = 0.5; neighborhood_radius = 2; intensity_thresh = 0; eccentricity_thresh = 0; im_mask = None; contrastLow = 50; contrastHigh = 200; darkline = False; intensity_clip_percent = 2; windows_curvature = [10,20,30]; minLineWidth = 8; maxLineWidth = 20; do_skeleton = True; do_enhance_contrast = True; prune_short = True; minimumBranchLength = 40.

Chemotaxis dataset

The chemotaxis dataset was provided by Jonna Alanko's group. The dataset contains live-cell images of dendritic cells migrated on CDMs. The one group contained chemotaxis gradient, while the other group contained control cells without a gradient. Live cell migration was imaged using a Nikon Eclipse Ti2-E widefield microscope

equipped with a 10× Plan Fluor objective. Time-lapse images were acquired every minute for a total duration of 10 hours.

The following values of parameters were used: single_frame = True; window_size = 50; overlap = 0.75; neighborhood_radius = 1; intensity_thresh = 0; eccentricity_thresh = 0; im_mask = None.

Statistical tests

To compare AFT-AI between two groups Mann-Whitney U test was used, the results of analysis were analyzed on normality using Kolmogorov-Smirnov test. For correlation analysis we used Pearson correlation. The number of repeats was equal two for brightfield and chemotaxis datasets, and one for Glioblastoma data.

3 Results and Discussion

3.1 Approaches for ECM description

Most tools for ECM description use a separate algorithm to extract ECM features, such as intensity-derivative algorithm, Fourier- and spectral-based algorithms, and directional-filter/transform algorithms. Each of these approaches can extract specific metrics that characterize the ECM variously. In AFT-tracks, we decided to apply two approaches: the intensity-derivative algorithm and the Fourier-based algorithm to describe local ECM properties, due to the effect of local areas on the nearby cells.

3.1.1 The FFT-based pipeline development

The FFT-based workflow

For fast and quantitative analysis of ECM orientation, we applied Fourier transformation analysis. We decided to use the AFT tool due to its rapid feature extraction and, compared with other tools, a low number of parameters for running (Marcotti et al., 2021). AFT-tracks breaks the FFT-based application into two steps: parameter definition and feature extraction, such as orientation, eccentricity, order, and AFT-AI - a measure of cell migration trajectory alignment with local ECM (see Materials and Methods for more details). To estimate how suitable the parameters are, AFT-tracks uses a preview image with the orientation of the fibers. Preview images visualized in the Jupiter notebook (**Fig. 9, A**) and saved in the Results folder (**Fig. 9, B**), giving users the opportunity to compare different parameter values and find the best one for their cases. After defining the parameters, users can apply the same set to all images in the experiment to extract ECM metrics and AFT-AI. The performed analysis can be saved as an output file in Spots format with a .csv extension, containing ECM metrics for each patch and AFT-AI for each cell step (**Fig. 9, C**).

A

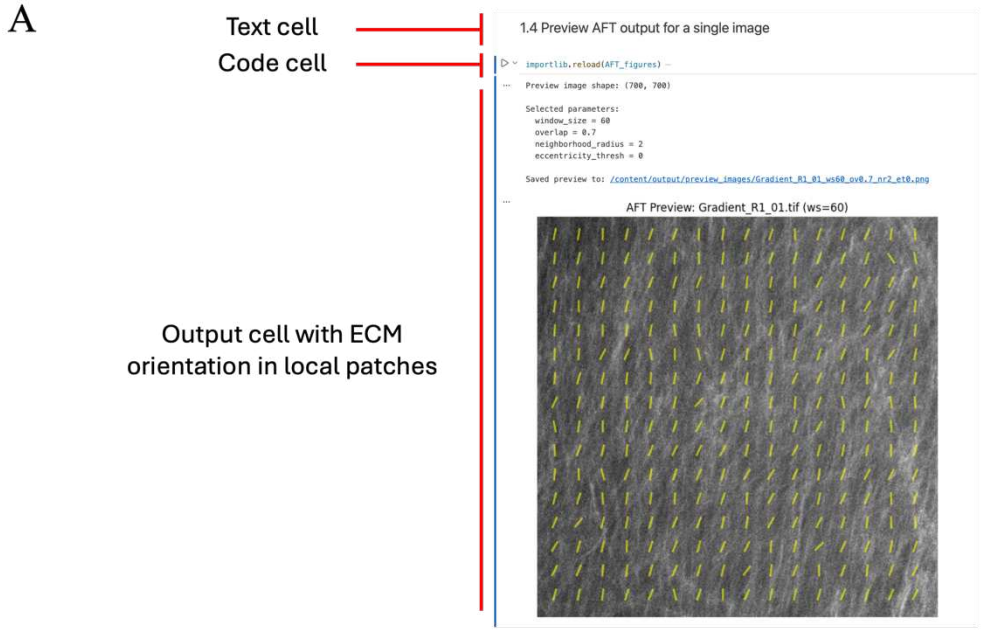

B

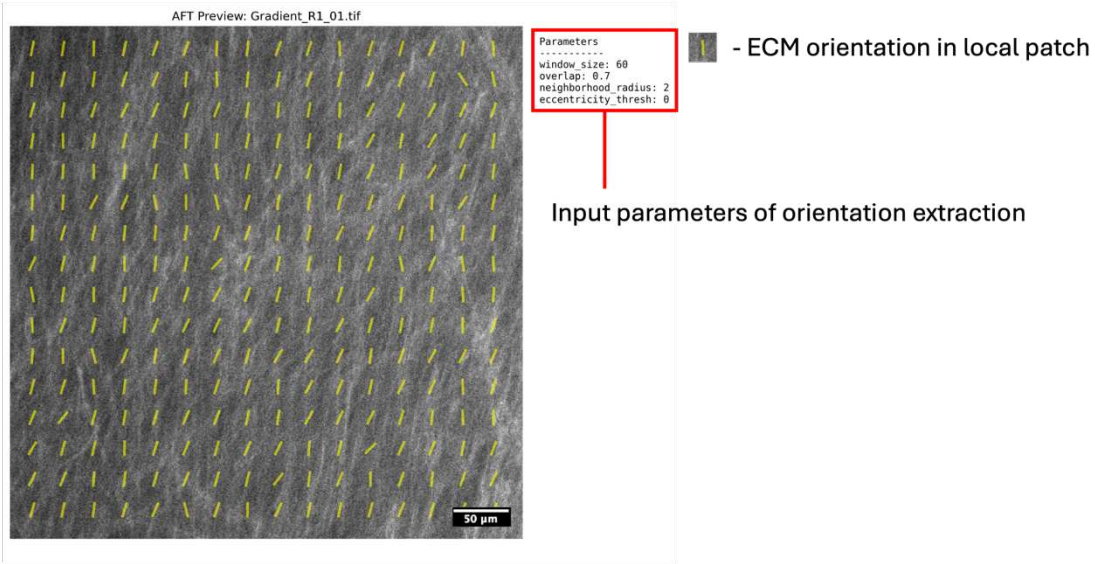

C

AD	AE	AF	AG	AH	AI	AJ	AK	AL	AM	AN	AO	AP	AQ
TRACK_ID	FRAME	POSITION_X	POSITION_Y	POSITION_Z	POSITION_T	Condition	AFT-AI	AFT_eccentricity	ECM_ID	order_value	window_size	overlap	neighborhood_radius
0	0	459.902124	608.168901	0	0	Gradient	0.89060029	0.489876059	ECM_282	0.96101379	50	0.75	1
0	1	459.763988	610.198369	0	60.2352104	Gradient	0.94862911	0.489876059	ECM_282	0.96101379	50	0.75	1
0	2	454.697934	600.87595	0	120.470421	Gradient	0.31212809	0.489876059	ECM_282	0.96101379	50	0.75	1
0	3	451.694316	604.37856	0	180.705631	Gradient	0.49431724	0.489876059	ECM_282	0.96101379	50	0.75	1
0	4	449.307459	608.528633	0	240.940842	Gradient	0.01162265	0.489876059	ECM_282	0.96101379	50	0.75	1
0	5	451.801012	607.54087	0	301.176052	Gradient	0.00450953	0.489876059	ECM_282	0.96101379	50	0.75	1
0	6	457.173384	606.440977	0	361.411263	Gradient	0.24312167	0.489876059	ECM_282	0.96101379	50	0.75	1
0	7	462.067424	607.672271	0	421.646473	Gradient	0.0010108	0.300669182	ECM_283	0.94614087	50	0.75	1
0	8	456.130553	610.220442	0	481.881683	Gradient	0.00197437	0.489876059	ECM_282	0.96101379	50	0.75	1
0	9	449.02514	612.524682	0	542.116894	Gradient	0.98836545	0.489876059	ECM_282	0.96101379	50	0.75	1
0	10	449.598196	616.051658	0	602.352104	Gradient	0.9476182	0.443504636	ECM_300	0.96629674	50	0.75	1
0	11	449.837928	636.311005	0	662.587315	Gradient	0.46769709	0.443504636	ECM_300	0.96629674	50	0.75	1
0	12	439.815364	651.777734	0	722.822525	Gradient	0.79211954	0.443504636	ECM_300	0.96629674	50	0.75	1

Figure 9. Output data from the FFT-based approach. A – Jupyter notebook structure and visualization of fiber orientation in a real ECM image; B – output figure showing FFT-derived parameters and local ECM orientation in each image patch (yellow lines); C – example of FFT-based metrics in the Spot table.

Tests of the AFT-tracks FFT-based approach on a synthetic dataset

To assess the capabilities of AFT-tracks to gain information about cell alignment with the ECM, I implemented an FFT-based pipeline on synthetic datasets, generated with manually written code that modulate fibers with different structural noise. Here, noise refers to randomly oriented structural fibers added to the synthetic ECM, which reduce the alignment of the matrix and increase disorder. Synthetic datasets contained three types of ECM under various structural noise conditions: high-noise, intermediate-noise, and low-noise ECM. Also, synthetic datasets contained three groups of cells with various migration behaviors: persistent, reversal, and random. Cells in the persistent group moved downward in the vertical axis, with only small changes in direction over time. In the reversal group, the overall movement was also directed downward, but cells occasionally switched direction for a few frames before continuing along the main path. In the random group, the direction of movement changed from frame to frame, showing the absence of persistent directional behavior (**Fig. 10**). For more information about the synthetic datasets generation parameters, see the Materials and Methods section.

The results of the synthetic dataset analysis showed that the values of the order and eccentricity metrics increased from the high-noise ECM to the low-noise ECM (**Fig. 11**). This confirms that uniaxially aligned ECM have higher order and eccentricity metrics than uniaxially unaligned ECM.

The AFT-AI increased in groups with persistent and reversal cell behavior as the ECM uniaxial alignment and structural noise decreased. In high noise, the ECM group of cells with persistent and reversal cell behavior have normally distributed values in the range [0, 1].

The AFT-AI in the group with random cell behavior has the same normally distributed values in the range [0, 1] for each ECM condition (**Fig. 11**). The synthetic test confirms that AFT-AI correctly describes cell-ECM alignment in different ECM and cell migration behavior conditions.

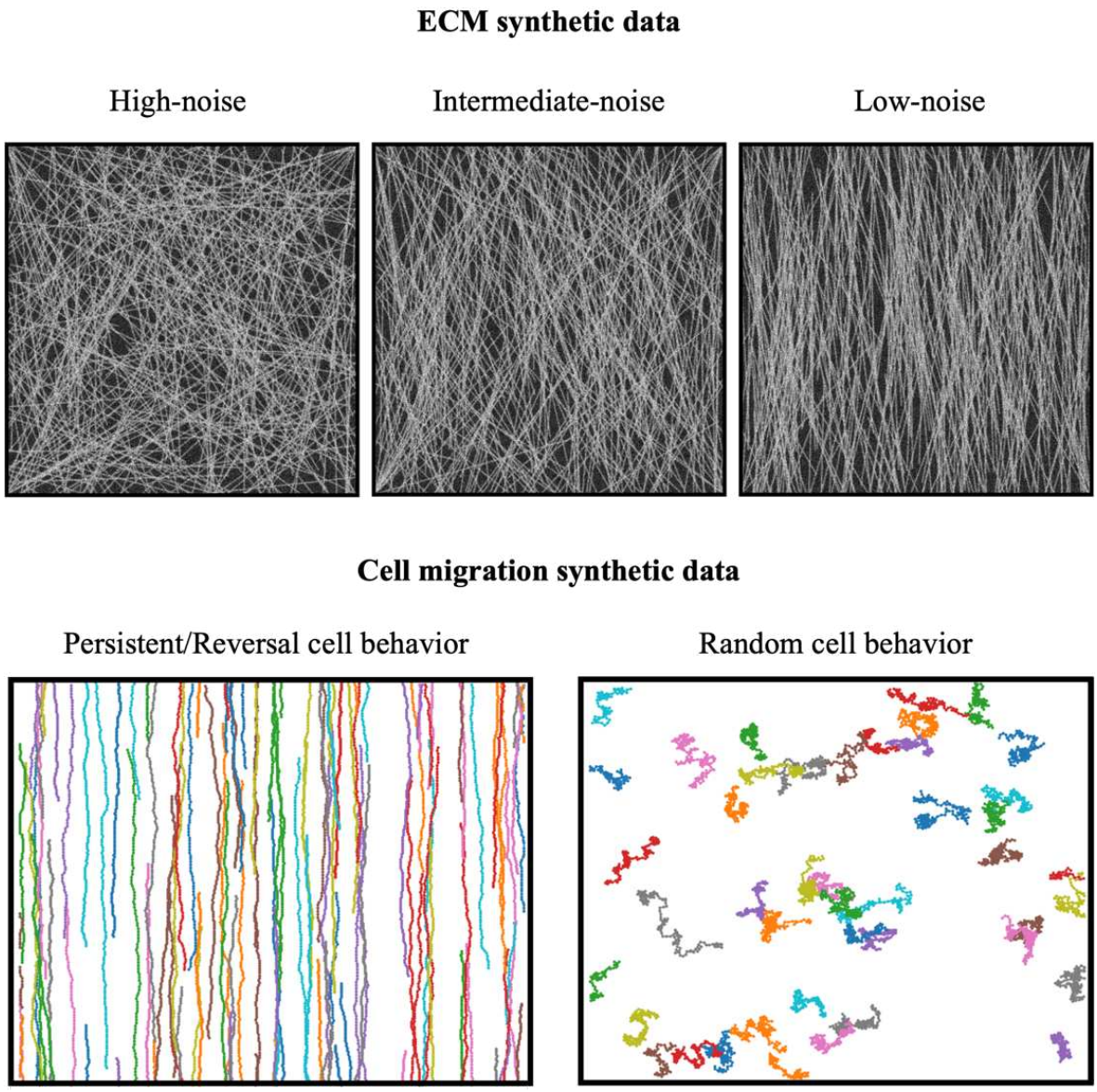

Figure 10. Synthetically generated datasets. The ECM data include different types of structural noise fibers. The cell migration data show individual cells (displayed in different colours) representing different migration behaviours.

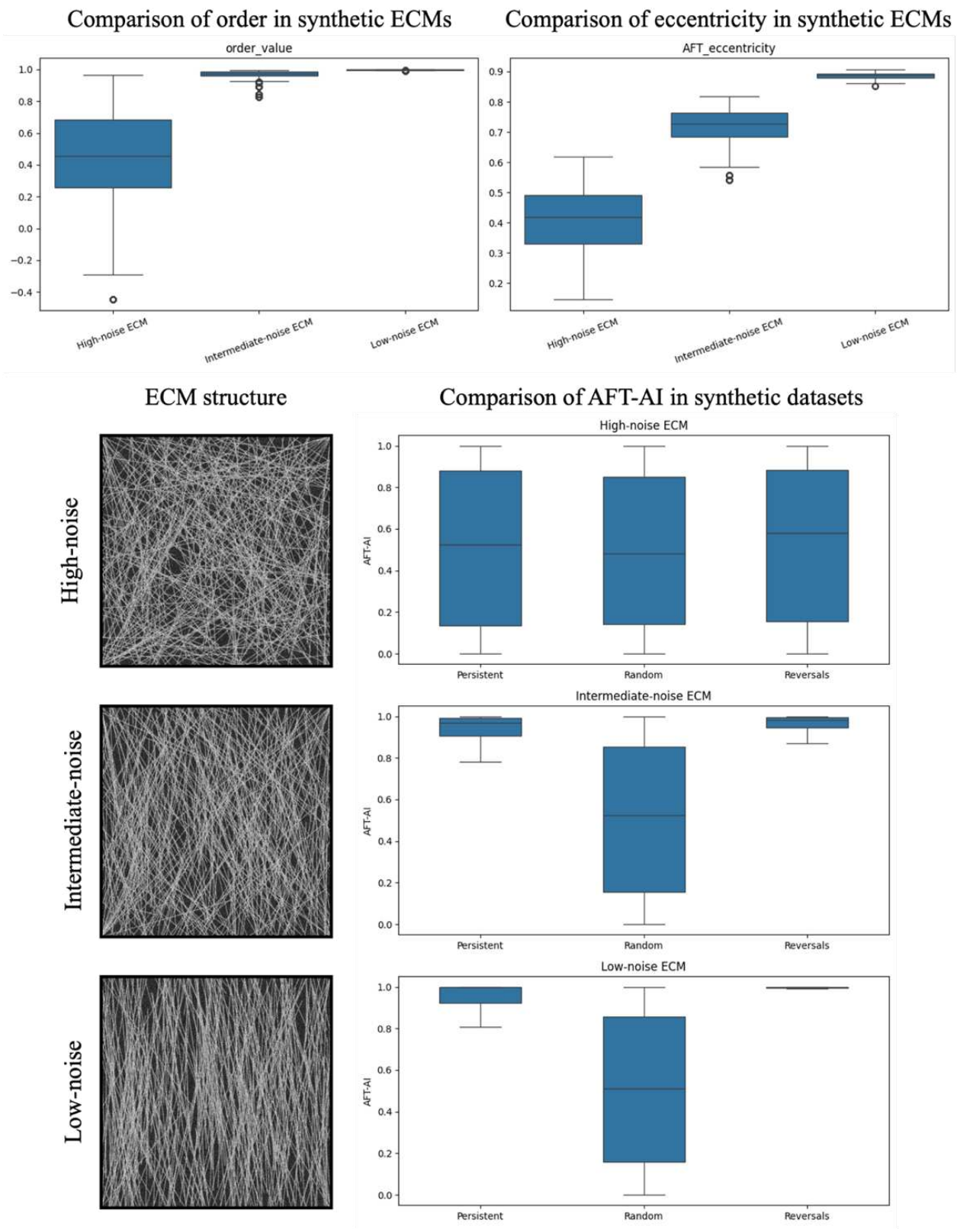

Figure 11. The comparison of FFT-based metrics of ECM and cell migration behavior in synthetic datasets. The white lines are fibers; the black is a background.

3.2 The segmentation-based pipeline development

3.2.1 Analysis of existing segmentation-based approaches

The FFT-based approach provides fast executable information about local ECM orientation. However, other structural parameters of the ECM cannot be extracted with Fourier transformation processing. These features include fractal dimension, pore size/porosity, fiber diameter, fiber length, fiber density, and number of branches and endpoints. To extract these features, we decided to implement a multiscale Ridge-detector that is commonly used to detect fiber-like structures. Unlike the FFT-based approach, which extracts ECM orientation features, the Ridge-detector approach provides a morphological pattern of the ECM. Notably, the segmentation-based approach is common in ECM segmentation tools, for example, TWOMBLI (Wershof et al., 2021), OrientationJ (Püspöki et al., 2016), and CT-FIRE (Bredfeldt et al., 2014).

Considering all tools for ECM segmentation, I was inspired by the TWOMBLY segmentation pipeline, which combines various FIJI plugins. This wide range of plugin approaches enables the extraction of various morphological metrics. Fundamentally, the TWOMBLI pipeline is an RD-based algorithm that segments fibers in images. The RD serves as an effective tool for detecting ridges and values in images. Thus, my decision was to construct a pipeline similar to the TWOMBLI segmentation workflow, based on available Python packages.

3.2.2 The development of the RD

The first step in development was analysis of the open-source TWOMBLI code. It helped me to understand how the pipeline works and how metrics are calculated. The TWOMBLI tool is based on the functionality of the Fiji RD plugin, which has a similar package in Python (https://github.com/lxfhfut/ridge-detector).

Unfortunately, the test of the existing python RD tool took many time to find appropriate parameters and did not provide the expected accuracy (**Fig. 12**). The combination of low accuracy and long processing time pushed me to test another RD package from scikit-image (https://scikit-

image.org/docs/stable/auto_examples/edges/plot_ridge_filter.html). This RD also did not provide the expected accuracy due to the absence of flexible parameters included in the Fiji plugin.

Due to the absence of a fast in parameter selection and accurate RD among available packages, I decided to write code to implement a simple, fast RD algorithm. The calculation of RD parameters, such as the lower and upper thresholds and sigma, was adapted from the Fiji RD plugin (https://imagej.net/plugins/ridge-detection). When choosing the algorithm's filtering method, I decided to use the highest eigenvalue after applying the Hessian filter to each pixel. That decision was based on the result of a comparison of different RD approaches by Shokouh et al., 2021.

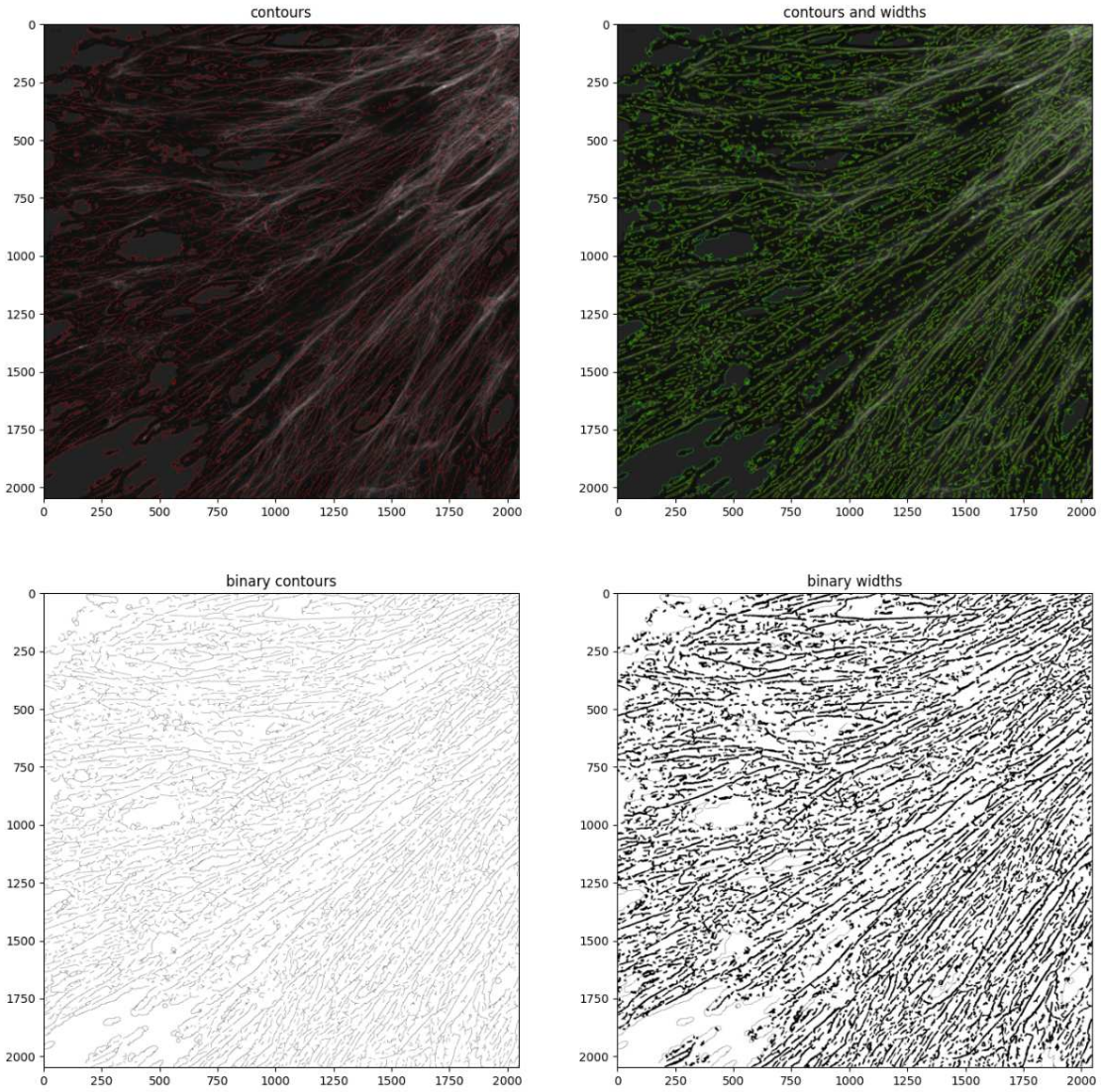

Figure 12. Example of ECM segmentation using the open-access RD packages.

Shokouh et al. described filtering using the highest eigenvalue as a “good compromise when the feature widths are growing”, which is well-suited to ECM images with various fiber widths. For more information about the manually written RD algorithm, see the Materials and Methods section.

3.2.3 Skeletonization and metrics extraction

To extract morphological information from detected fibers, I implemented the skeletonization and metrics linked with the ECM pattern. The skeletonization provides the structural pattern of detected fibers. Additionally, after implementation of segmentation and skeletonization, I realized that RD generates false-positive (FP) results in dark areas and out-of-focus fibers.

To exclude these FP results, I decided to implement two approaches: create a binary mask of background pixels and apply a filter that excludes branches based on their type and length (**Fig. 13**). To generate a mask with background pixels, I used the ilastik tool (Berg et al., 2019) that successfully segments background areas.

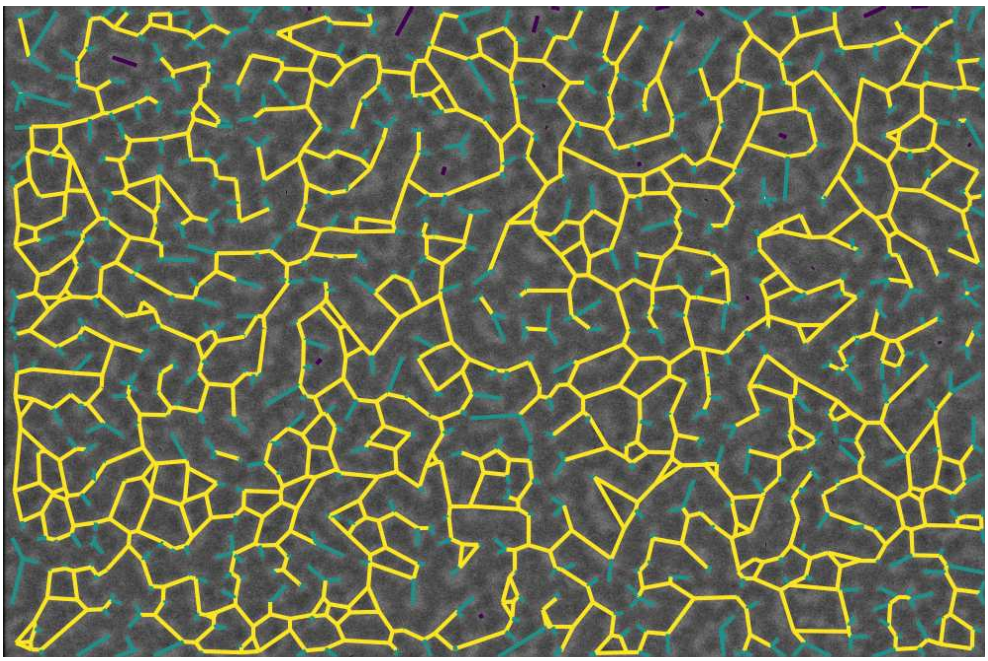

Figure 13. Illustration of classification of branch types: yellow - junction-to-junction branches, blue – junction-to-endpoints branches, violet – separated endpoint-to-endpoint objects. Illustration adapted from Skan documentation (skeleton-analysis.org).

To exclude short branches in out-of-focus fibers, I initially implemented CCL, which helped me exclude small, separated objects within the ECM network. However, the CCL was not suitable to exclude short branches within the ECM network. To solve this problem, I implemented the Skan library, which can classify the ECM branches and junctions within the ECM net (see Materials and Methods for details). This approach helped me to exclude short branches after the RD mask skeletonization.

3.2.4 Segmentation approach tests

To test the effect of various parameters in the segmentation approach, I modified the following parameters: “lowContrast”, “highContrast”, “minimumBranchLength”, “minLineWidth”, and “maxLineWidth”.

The “lowContrast” and “highContrast” define the lowest and highest grayscale values of the detected lines. The modification of these parameters affects the RD response and, hence, the fibers included in further analysis. As shown in **Fig. 14**, the range [0, 50] includes both the main fibers and the low-intensity fibers. The range [50, 100] excludes some low-intensity fibers, making the mask clearer than the range [0, 50]. The range [200, 255] includes fibers from the darkest part of the image, which are mostly FP results. The test showed that changes in parameters affect the RD response and can change detection accuracy (**Fig. 14**, blue area).

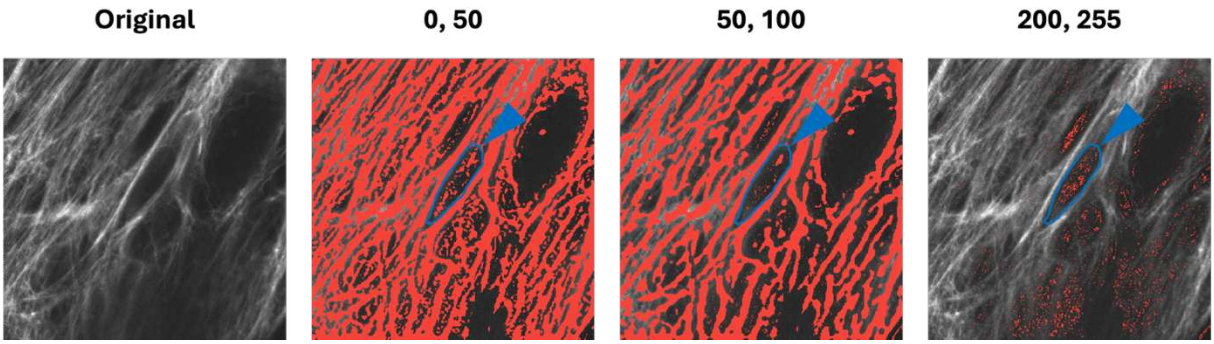

Figure 14. Effect of the "lowContrast", "highContrast" modification on the segmentation results. Blue area refers to the FP results of the detection.

The “minBranchLength” defines a low threshold for the length of the branches and excludes FP results of the detection (**Fig. 15**, red circle area). However, the objects

separated from the ECM network are not excluded after minBranchLength filtering, as illustrated in the blue circle area in **Fig. 15**. The test results indicate the low accuracy in filtering of FP segmentation results, specifically for separated ECM fiber elements.

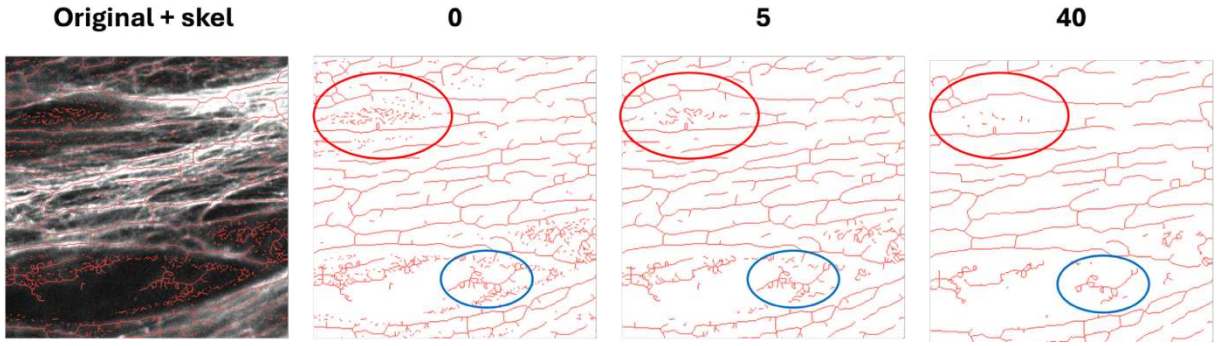

Figure 15. Effect of "minBranchLength" modification on skeletonization filtering. The red-circled area indicates the FP results of the segmentation. The blue-circle area denotes objects separated from the ECM network.

I linked this unsensitivity of the filtering tool with the absence of CCL filtering. In future development of the tool, I plan to add CCL filtering to the RD mask extraction and combine CCL- and Skan-based filtering in the skeletonization step. Additionally, I plan to implement multiple filtration repeats during Skan-based filtering, which should help exclude multibranch FP results, as schematically illustrated in **Fig. 16**.

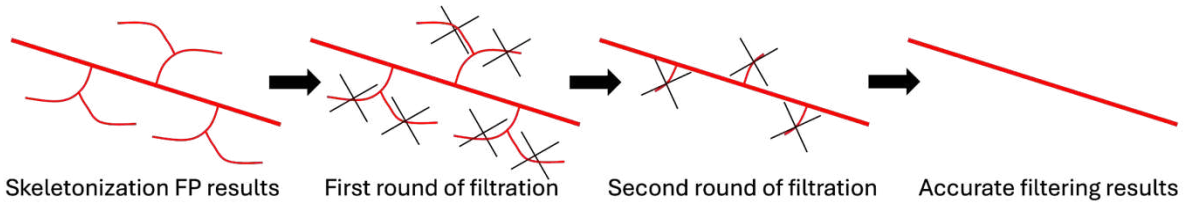

Figure 16. Schematic explanation of the multi-round filtering method. Multiround application of Skan-based approach can exclude FP results.

The “minLineWidth” and “maxLineWidth” define the minimum and maximum widths of the lines detected on the images. The changes in these parameters affect the number of detected lines. The test results showed that “minLineWidth” equal 0 leads to oversensitivity and inaccurate segmentation results. At the same time, as the

“minLineWidth” threshold increases, the segmentation results retain only branches with high line width (**Fig. 17**).

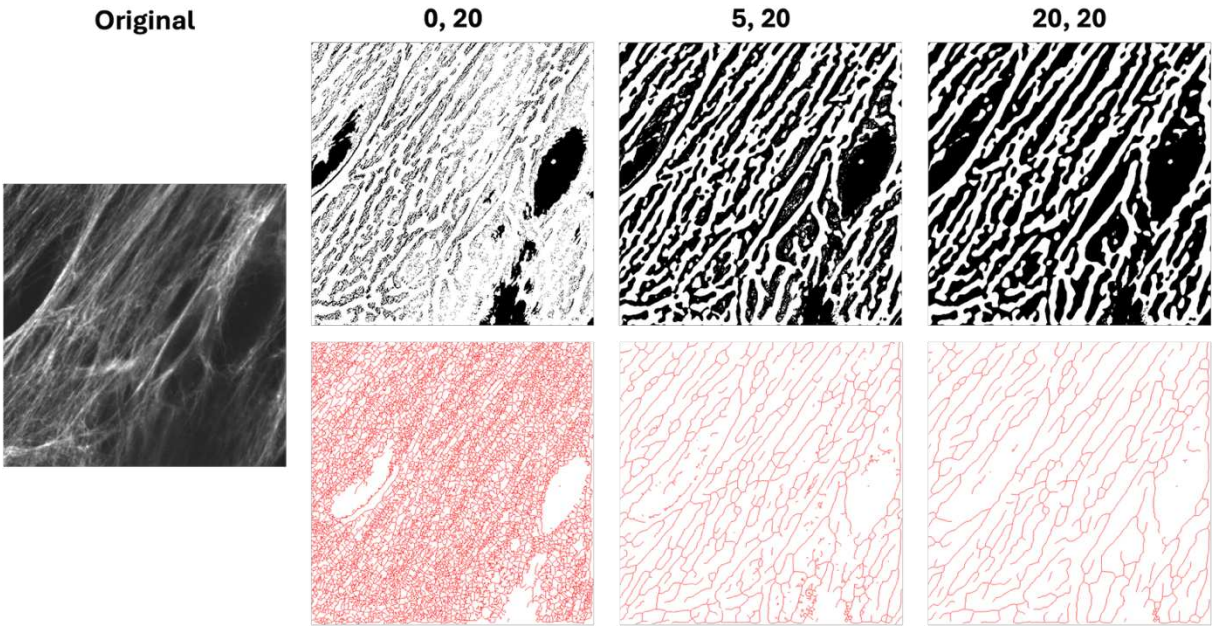

Figure 17. Effect of "minLineWidth", "maxLineWidth" on the segmentation and skeletonization results. The increasing of the "minLineWidth" value exclude small branches.

After tests, it is clearly seen that the current RD has a limitation: the low-width lines that overlap with high-width lines are excluded from the final RD mask after merging (**Fig. 18**), hence, only small fibers that are not overlapped with high-width lines are included in the analysis.

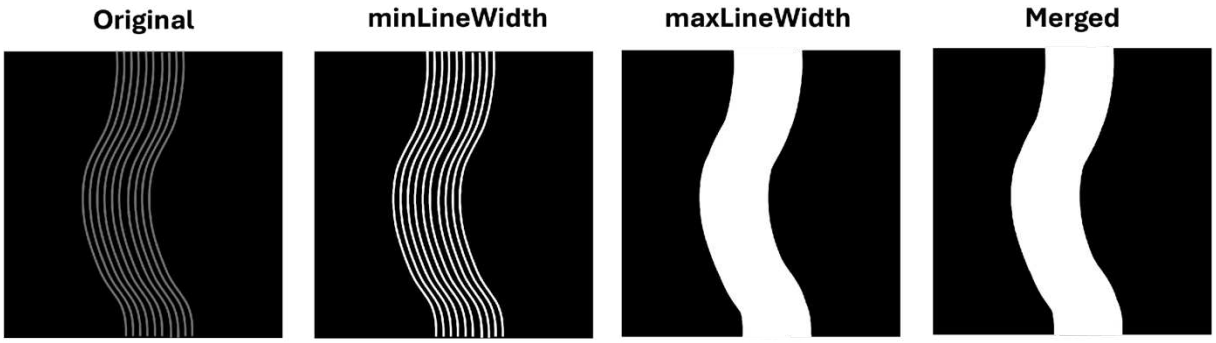

Figure 18. Schematic illustration of the overlapping of detected lines with different LineWidth.

The tool's results showed that the segmentation-based approach performed the main function of extracting the ECM pattern and could be used for further metric extraction. However, the filtering algorithm and merging step of RD masks require further improvement. In the following section, I tried to extract features to test how metric values reflect real ECM properties.

3.3 Segmentation metrics development

Following the development of the segmentation approach, my goal was to extract quantitative metrics that characterize the ECM pattern. I decided to exclude the intensity, lacunarity, $N_{branchpoints}$, $N_{endpoints}$, HDM, FFD, and curvature metrics (see Materials and Methods for details).

The intensity metric provides the mean intensity of the matrix. It is particularly useful when combined with ECM-sensitive dyes, which can, for example, indicate the concentration of ECM components in the region. The lacunarity metric quantifies the local heterogeneity of gray levels, representing the number of gaps in the matrix. HDM provides information about the part of the area occupied by ECM.
The $N_{branchpoints}$ and $N_{endpoints}$ metrics provide information about the number of junctions and fiber ends present in each ECM patch. Importantly,
the $N_{branchpoints}$ and $N_{endpoints}$ values describe the RD segmentation pattern and indirectly represent information about the real number of fiber branches or endpoints. The FFD provides information about the structural complexity of the ECM. I selected the box-counting mode, which was imported from the existing FFD tool developed by Cui et al. (2024) (https://github.com/wanglab-georgetown/fractal). Thus, the more complex and branched the structure is, the higher the number of boxes will be included in this structure, and the higher value of the FFD metric will be (**Fig. 19**). The curvature metric provides information about the straightness of the fibers in the patch. The values are normalized by the fiber length, making this metric suitable for comparison across different experimental groups.

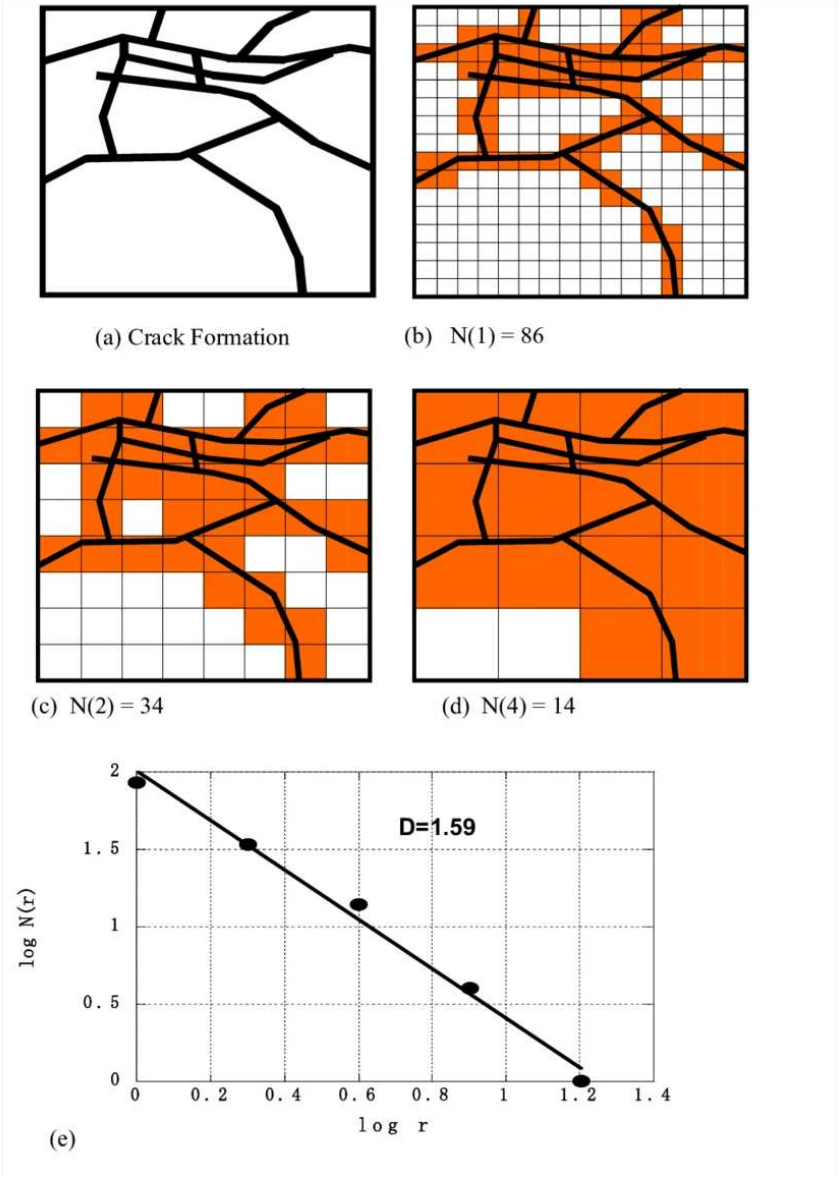

Figure 19. Fractal Dimension by Box Counting Method. Illustration adapted from Mihashi et al., 2014.

3.4 Segmentation metrics tests

To test segmentation metrics, I used the Glioblastoma dataset, which contains super-resolution images of the ECM. The high resolution helps to segment fibers more precisely. The intensity metric reflects the mean intensity in the ECM. Thus, the top patch in **Fig. 20** has a higher value and collagen dye signal than the bottom one.

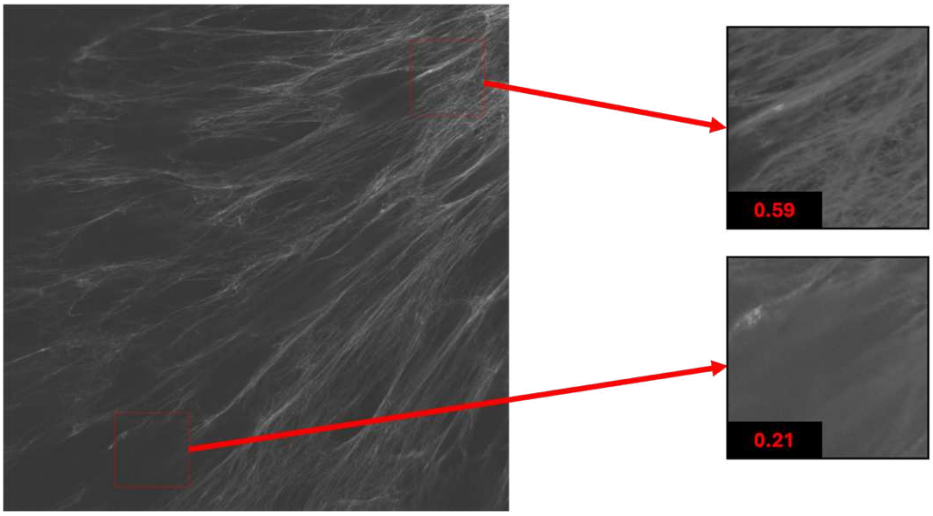

Figure 20. Result of the intensity metric test.

The results of the lacunarity metric test reflect the number of gaps in the ECM. Thus, the top patch in **Fig. 21** has fewer gaps and, hence, a lower lacunarity value than the bottom patch.

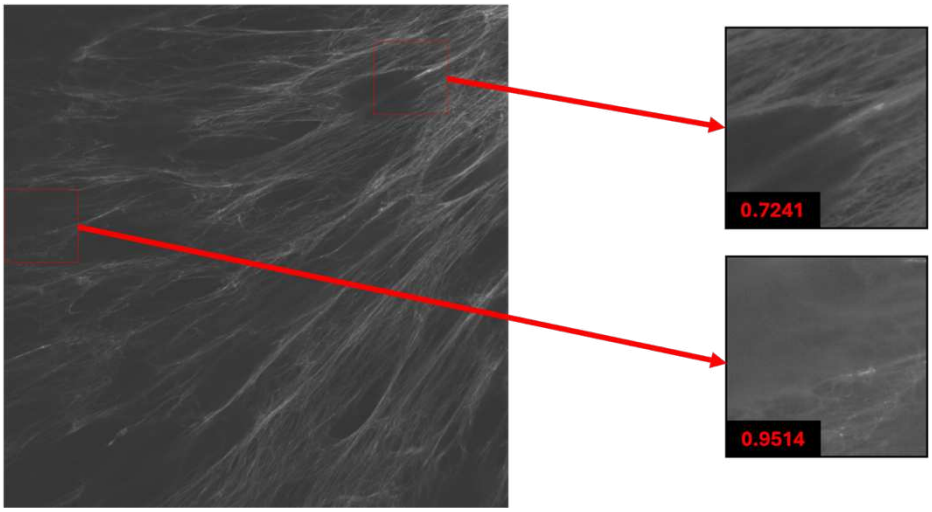

Figure 21. Result of the lacunarity metric test.

The results of the HDM metric test reflect the part of the fibers that occupied the ECM. Thus, the top patch in **Fig. 22** has more fibers and, hence, a higher HDM metric value than the bottom patch.

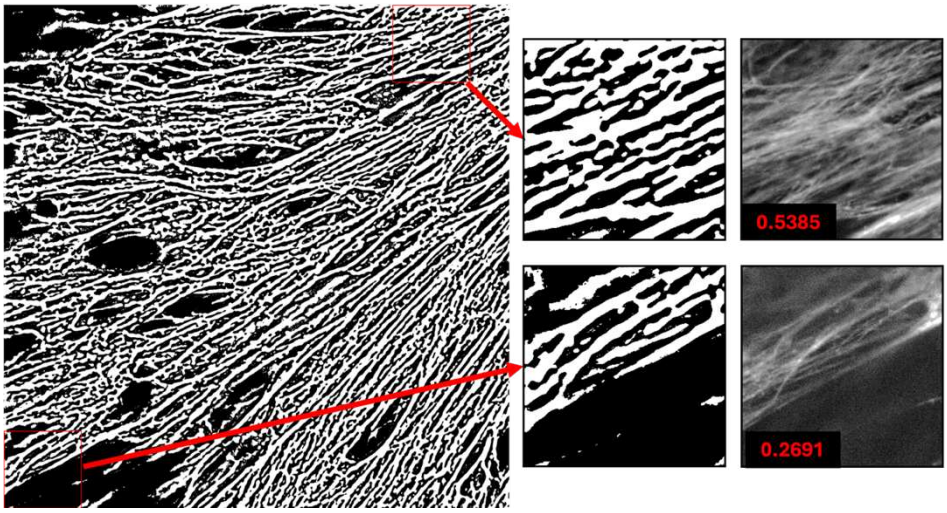

Figure 22. Result of the HDM metric test.

The results of $N_{branchpoints}$ metric test reflect the number of junctions in the ECM. Thus, the top patch in **Fig. 23** has fewer $N_{branchpoints}$ than the bottom one.

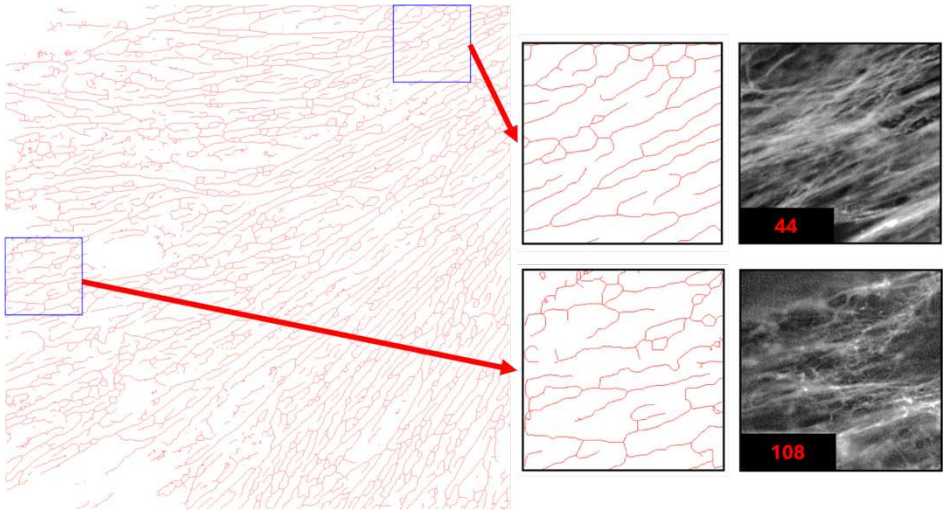

Figure 23. Result of the $N_{branchpoints}$ metric test.

The results of $N_{endpoints}$ metric test reflect the number of ended fibers in the ECM. Thus, the top patch in **Fig. 24** has fewer $N_{endpoints}$ than the bottom one.

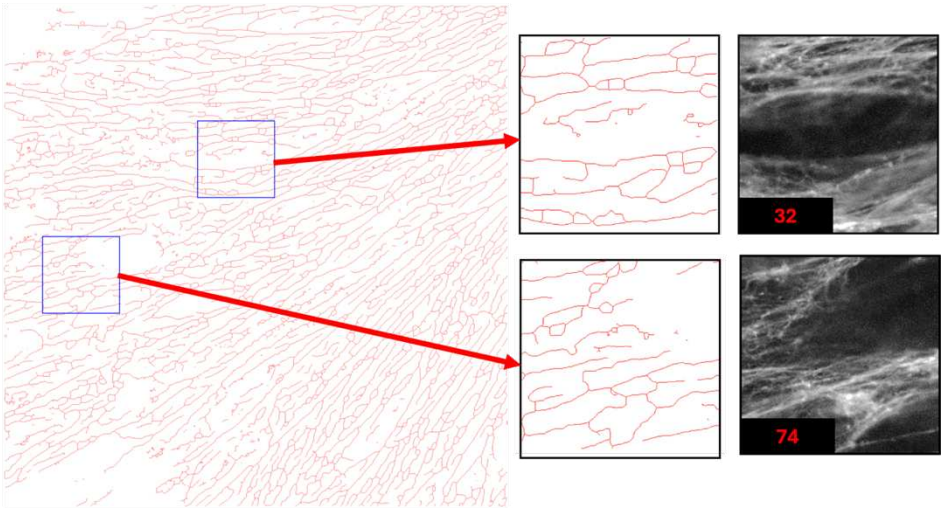

Figure 24. Result of the $N_{endpoints}$ metric test.

Despite the correspondence of $N_{branchpoints}$ and $N_{endpoints}$ results with the ECM state, the thin ECM fibers are segmented with low accuracy. Additionally, there are FP results in areas with out-of-focus fibers (**Fig. 25**). These inaccuracies reduce the trustworthiness of the $N_{endpoints}$ or $N_{branchpoints}$ metrics and require further improvement through changes to RD and filtration algorithms. However, the $N_{endpoints}$ and $N_{branchpoints}$ metrics represent the numbers of junctions and endpoints in the ECM, which, together with other metrics, serve as a solid foundation for ECM description.

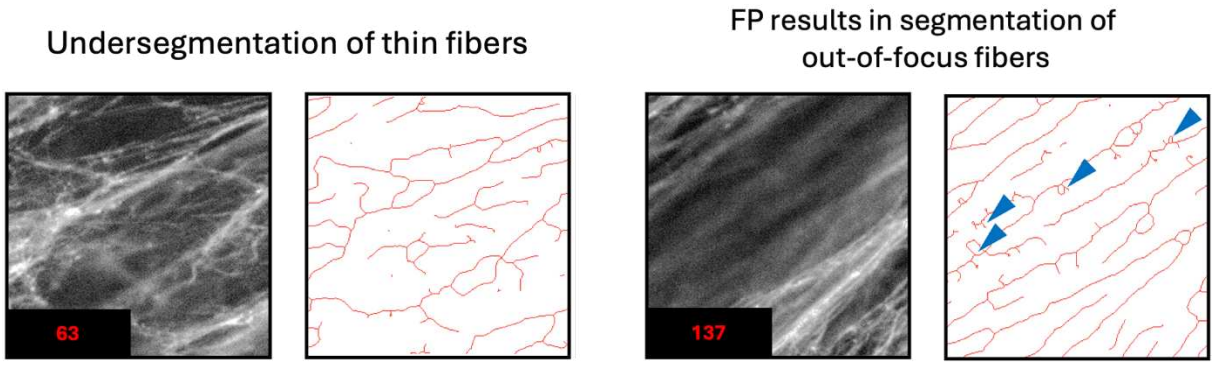

Figure 25. Undersegmentation of thin fibers and FP results in segmentation of out-of-focus fibers. The blue arrows refer to FP results.

The FFD metric results reflect the complexity of the ECM pattern. Thus, the top patch in **Fig. 26** has a more complex network compared to the bottom patch.

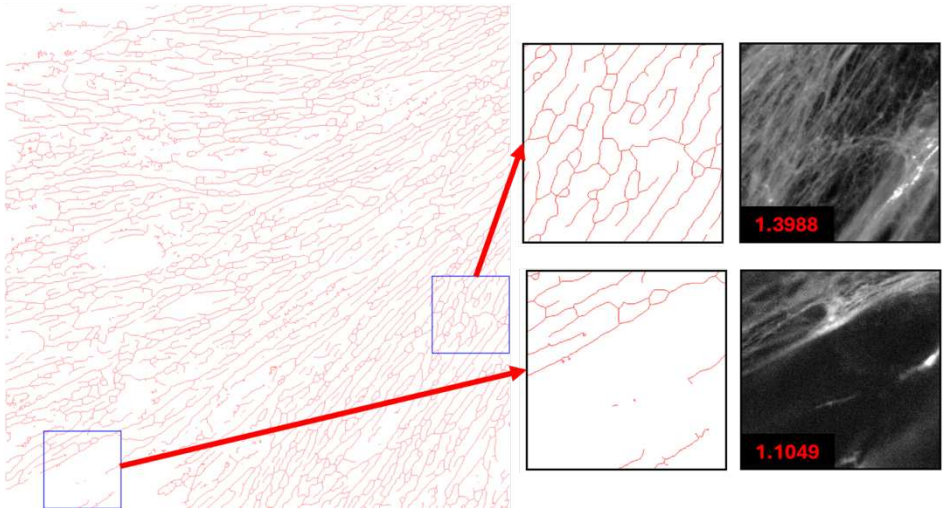

Figure 26. Result of the FFD metric test.

The curvature metric results reflect the straightness of the ECM fibers. Thus, the top patch in **Fig. 27** has fewer straight branches, and, hence, a higher number of curvatures, compared to the bottom patch.

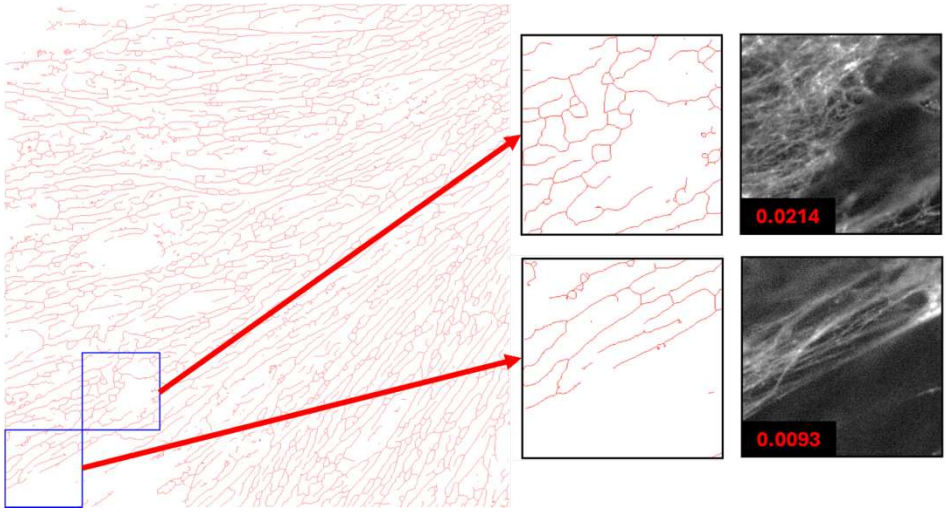

Figure 27. Result of the curvature metric test.

Overall, the segmentation-based metrics test confirmed the algorithm's applicability to ECM description. Despite inaccuracy in some specific cases, the metrics represent the ECM structural pattern and can be used in experimental datasets, which was the next part of the AFT-tracks development.

3.5 Cell migration metrics implementation on the patch level

After the extraction of ECM features, I focused on the extraction of cell migration metrics in the local patch level to connect local ECM properties with changes in cell migration behavior. The extraction of cell migration metrics based on CellTracksCollab functionality. The CellTracksColab provides two approaches for describing cell migration behavior: track-level metrics and spot-level metrics calculated using a rolling window. The rolling window approach computes an average over the following spots within the window.

During the implementation of the track-level metrics, I realized that directly implementing them caused inaccurate calculations in patches because cells exited and re-entered a patch. To avoid this issue, tracks were split into segments inside the patch. The mean values of all segments within the patch were then computed. In addition to the CellTracksColab application, AFT-tracks implements the new metrics at the spot-level (see Materials and Methods for details).

Following the implementation of cell migration metrics, I investigated how these metrics correlate with ECM features. Thus, the next step in tool development was the test of the AFT-tracks on real experimental data.

3.6 Experimental data processing

To test the AFT-tracks application on real experimental data, we decided to take live-cell imaging datasets imaged with various microscopes and resolutions. The various experimental conditions support the applicability of AFT-tracks for a wide range of cell migration assays. Additionally, a high-resolution dataset provides an opportunity to compare FFT- and segmentation-based approaches.

3.6.1 Brightfield dataset

Brightfield microscopy cell migration data on cell-derived matrices (CDMs) were taken from a previously published study about the role of L-type calcium channels in filopodia stabilization during invasion (Jacquemet et al., 2016). One group contained untreated cells, while the other group contained Carboxyamidotriazole-treated cells. The AFT-

tracks can help reveal the alignment of ECM and cells after treatment, reflecting the number of filopodia, one of the main components of cellular migration.

The comparison of the two groups reveals a significant difference in cell alignment with the ECM between the two conditions (**Fig. 28**). Thus, Untreated cells were more aligned with the ECM than Carboxyamidotriazole-treated cells.

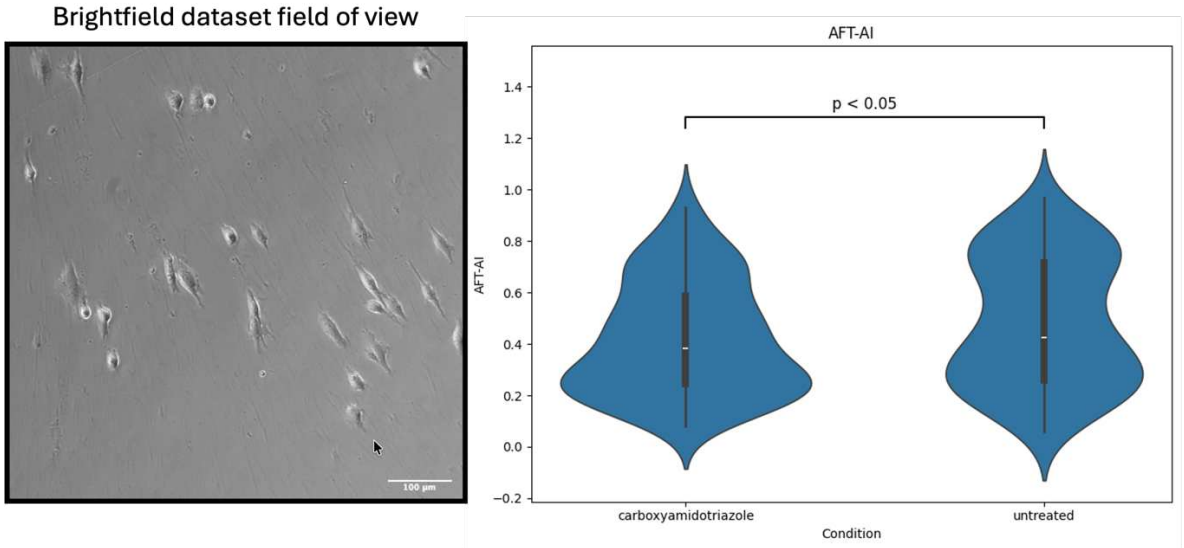

Figure 28. Example of the brightfield dataset and comparison of AFT-AI between the two groups in the brightfield dataset. Sample size: 2 per group. Groups were compared using a Mann-Whitney U test to evaluate differences in AFT-AI values.

Correlation analysis showed that cell morphology exhibited stronger correlations with AFT-AI and ECM features in treated cells compared with untreated cells, which demonstrated weaker correlations between morphological features and AFT-AI and ECM characteristics (**Fig. 29**). An exception was the “ellipse_theta” feature. This metric describes the spatial orientation of the cell's major axis. The results indicate that cells are less aligned with the ECM when their major axis is oriented horizontally.

Overall, the analysis results support the original study and provide an additional perspective for interpreting results through the cell-ECM interplay. Thus, based on the data, I speculate that treated cells are more aligned with the ECM and exhibit greater morphological flexibility during alignment than the untreated group.

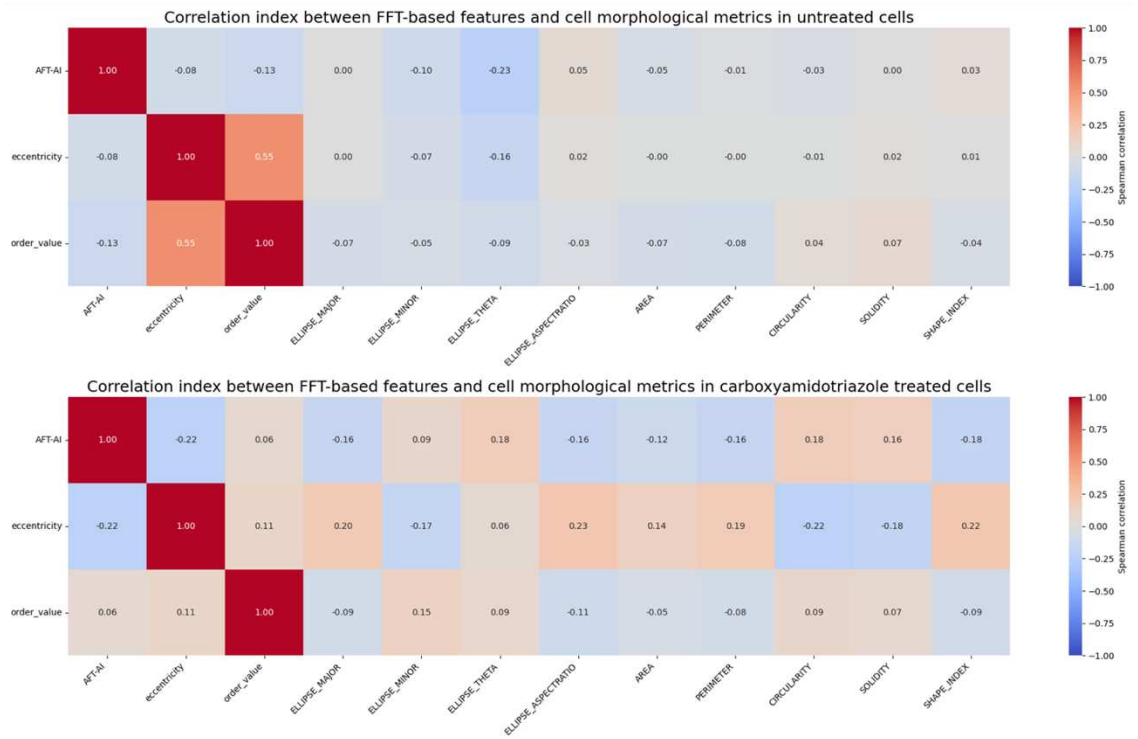

Figure 29. Correlation index between FFT-based metrics and cell morphology metrics in the brightfield dataset.

3.6.2 Glioblastoma dataset

Glioblastoma fluorescent microscopy cell migration data on CDMs were taken from a study about the role of CCT8 in MYO10-positive filopodia formation (Popovich et al., unpublished data). One group contained control cells, while the other group contained siCCT8 cells. The glioblastoma dataset contained super-resolution images with separated fibers, making them suitable for testing both FFT- and segmentation-based approaches. The AFT-tracks was used to reveal how silencing of CCT8, which leads to less filopodia formation, can reflect on alignment with the ECM.

Firstly, the analysis of the data reveals that FFT- and segmentation-based approaches do not work accurately with ECM images that contain signals from other channels. These showed that AFT-tracks require a clear ECM signal without cross-talk with other channels.

Secondly, I analyze AFT-AI in each condition. The compression results showed that cells in the siCCT8si5 group were more aligned with the environment than control cells (**Fig. 30**). These results suggest that siCCT8 depends more on the ECM after loss of CCT8.

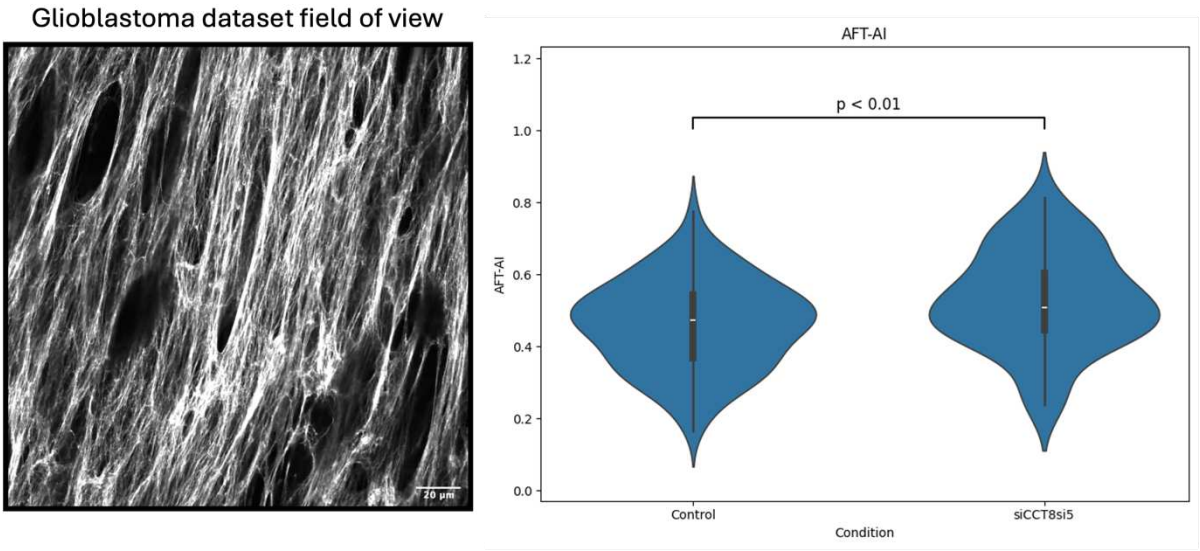

Figure 30. Example of the glioblastoma dataset and comparison of AFT-AI between the two groups in the brightfield dataset. Sample size: 1 per group. Groups were compared using a Mann-Whitney U test to evaluate differences in AFT-AI values.

Thirdly, I analyzed cell migration metrics and compared track- and spot-level rolling-window approaches. The analysis of cell migration behavior revealed differences in the spot-level rolling window and the track-level approach (**Fig. 31**).

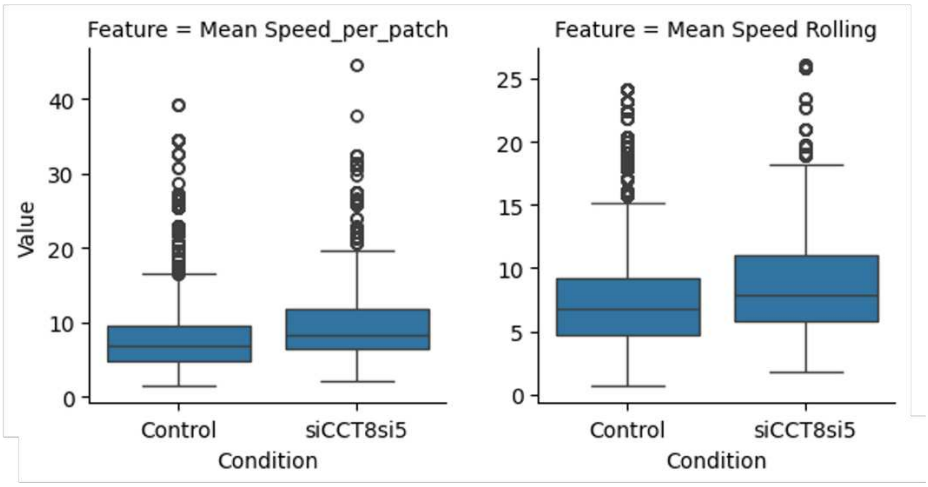

Figure 31. The difference in track-level and spot-level metrics. Mean speed per patch metrics include more outliers that Rolling approach.

Thus, almost every feature has a different range across the two approaches. I linked it with the limitations of the rolling window approach: the rolling window does not calculate the metric for the last spots of the tracks, and track-level metrics include all

spots inside the patch. Noticeably, the distribution of metrics was the same, indicating that the two approaches describe the dataset in the same way.

However, I think two approaches could be useful in specific cases. For example, if the dataset contains many short tracks, it is more useful to use per-segment mean values that do not exclude the final positions. If the dataset contains long tracks travelling from patch to patch, it will be useful to use a rolling-window approach to calculate metrics per spot, rather than excluding short segments during track filtering in the patch.

Finally, I analyzed the correlations between cell migration metrics and ECM parameters. In contrast to the brightfield dataset, the correlation analysis did not reveal a significant correlation between AFT-AI and ECM features. However, several cell migration metrics showed weak correlations with ECM features (red box in **Fig. 32**).

In particular, I want to focus on two migration metrics: “Mean_Speed_per_patch” and “Spatial_Coverage_per_patch”. The “Mean_Speed_per_patch” metric in the siCCT8 group showed weak correlations with ECM eccentricity, intensity, and order value, suggesting that ECM structural features may have a stronger influence on cell speed.

The correlation between “Spatial_Coverage_per_patch” and ECM metrics in the siCCT8 group indicated that cells occupy a larger area during migration in highly eccentric, dense matrices. This observation may suggest that, in the absence of filopodia, siCCT8 cells rely more heavily on the ECM structure to guide their migration.

Additionally, lacunarity showed a negative correlation with spatial coverage, suggesting that the presence of lacunes in the matrix limits the spatial spread of siCCT8 cells during migration.

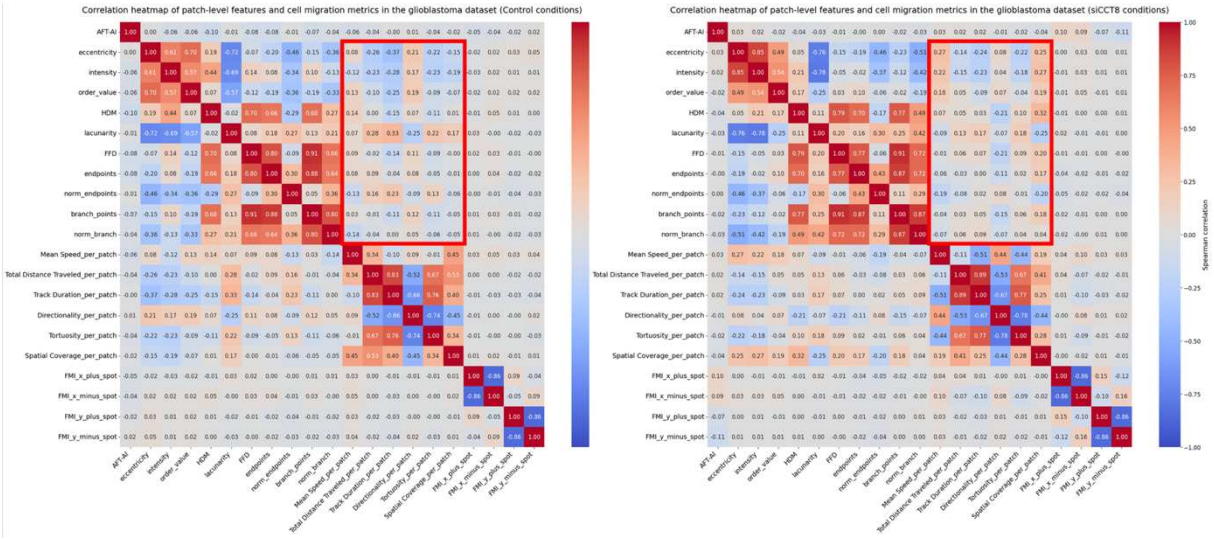

Figure 32. Correlation between ECM metrics and cell migration metrics in the glioblastoma dataset. The red box highlights the metrics with the most difference in correlation.

Additionally, the correlation analysis of ECM features indicated that FFT- and segmentation-based approaches complement each other (**Fig. 33**). This is supported by the lack of strong correlation between metrics from the two approaches, and their conceptual relation. For example, the lacunarity metric was strongly negatively correlated with eccentricity, norm_endpoints, and norm_branch metrics. This is consistent with the fact that an ECM highly structured along one axis contains fewer lacunes, endpoints, and branch points.

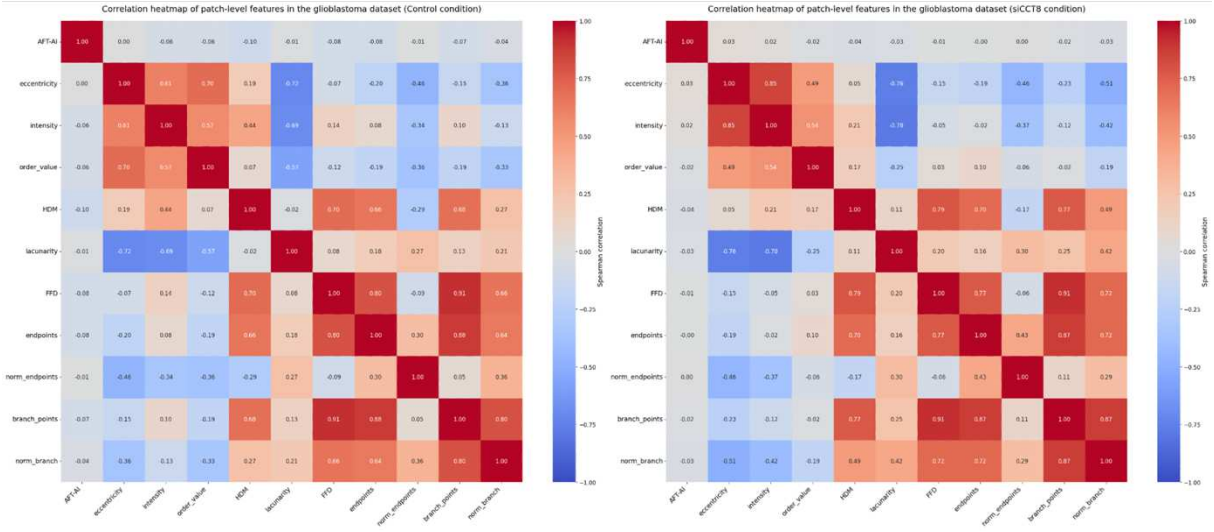

Figure 33. Correlation between FFT- and segmentation-based ECM metrics in glioblastoma dataset. The FFT- and Segmentation-based approaches do not have strong correlation that indicate different description of the ECM with two approaches.

3.6.3 Chemotaxis dataset

Chemotaxis cell migration data on CDMs were obtained from a study on the role of chemotactic cues in dendritic cell migration (Weinzettl et al., unpublished data). One group contained control cells in uniform conditions, while the other group contained dendritic cells with a chemotaxis cue on the right side of the CDMs. The AFT-tracks was used to reveal any changes in cell alignment in the presence of ECM and a cue.

The results of the analysis showed that cells in the Gradient group were more aligned with the ECM and moved in the cue direction compared with the Uniform condition (**Fig. 34**). Cells in the Uniform condition migrated more stochastically and were less aligned with the ECM. The results suggest that alignment with ECM regulates directed cell migration to the cue, showing that AFT-tracks can be suitable for this type of analysis.

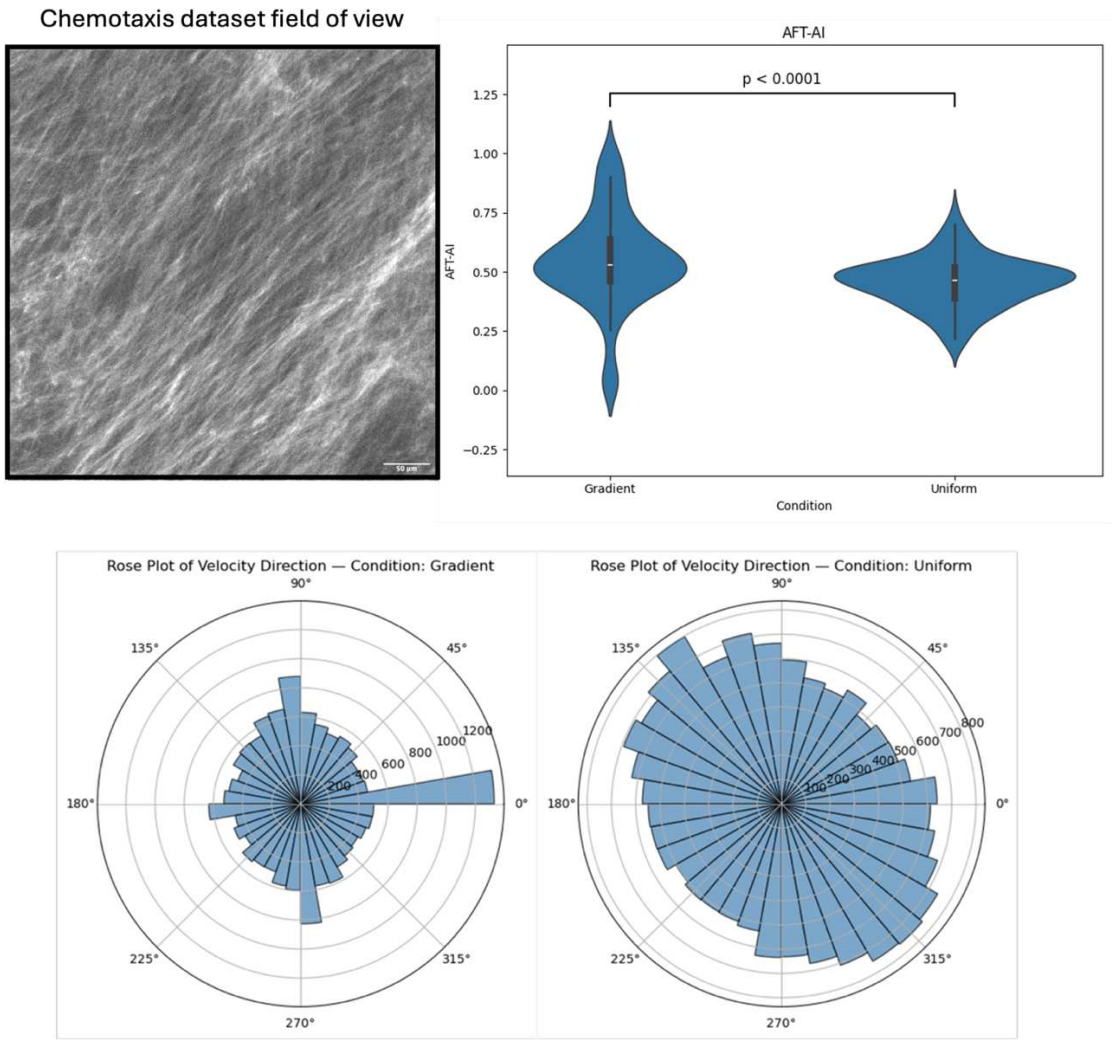

Figure 34. AFT-AI and directionality rose plot for chemotaxis dataset. Sample size: 2 per group. Groups were compared using a Mann-Whitney U test to evaluate differences in AFT-AI values.

3.7 Adaptation of the AFT-tracks to local running

The online and open-source platforms with a Jupyter-like structure (e.g., Google Colab) have limited computational resources, which makes it challenging to analyze massive data. To address this challenge, we decided to switch the AFT-tracks to local execution.

The local version of the tool was implemented using the LabConstructor framework (Ivan Hidalgo et al., unpublished data). LabConstructor enables the transformation of Colab notebooks into a single executable file that can be installed locally and opened in the Jupyter Notebook application.

The AFT-tracks tool was successfully installed locally using an executable generated with LabConstructor (**Fig. 35**). In this setup, users do not need to manually install Python packages or Conda environments, making the tool accessible to a wide range of users and avoiding the resource limitations of Google Colab.

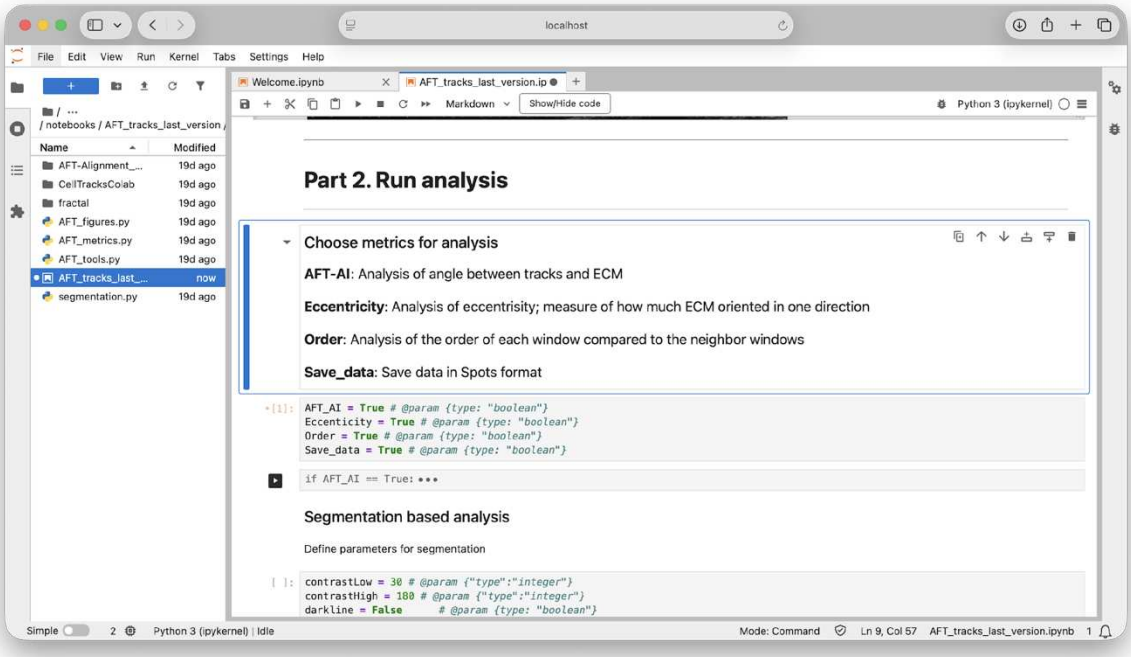

Figure 35. The interface of AFT-tracks running in a local Jupyter Notebook environment.

4 Conclusion

Cell migration plays a crucial role in key processes in living organisms, and in recent years, researchers have focused on the communication between migrating cells and the ECM. In this thesis, I began developing AFT-tracks – an open-source, user-friendly tool for describing the interplay between cells and the ECM. The result of this work was the development of the AFT-AI metric, which describes the alignment of cells with the surrounding ECM. I also validated AFT-AI's functionality on both synthetic and real datasets. Also, I developed two main approaches to ECM description: FFT and RD. Each of these approaches complements the others and describes a different characteristic of ECM. Additionally, I tested AFT-tracks across various datasets and identified new space to reveal cell-ECM interplay during data interpretation. In the final step, I built a pipeline to adapt the tool for local and Google Colab environments, making it accessible to a wide range of users and use cases.

5 References

Alonso-Matilla, R., Provenzano, P.P., Odde, D.J., 2025. Physical principles and mechanisms of cell migration. npj Biological Physics and Mechanics 2025 2:1 2, 1–9. https://doi.org/10.1038/S44341-024-00008-W

Beltman, J.B., Marée, A.F.M., De Boer, R.J., 2009. Analysing immune cell migration. Nature Reviews Immunology 2009 9:11 9, 789–798. https://doi.org/10.1038/nri2638

Bhattiprolu, S., 2025. AI-driven microscopy: from classical analysis to deep learning applications. Methods in Microscopy 2, 153–163. https://doi.org/10.1515/MIM-2024-0033

Boudaoud, A., Burian, A., Borowska-Wykręt, D., Uyttewaal, M., Wrzalik, R., Kwiatkowska, D., Hamant, O., 2014. FibrilTool, an ImageJ plug-in to quantify fibrillar structures in raw microscopy images. Nature Protocols 2013 9:2 9, 457–463. https://doi.org/10.1038/nprot.2014.024

Bredfeldt, J.S., Liu, Y., Pehlke, C.A., Conklin, M.W., Szulczewski, J.M., Inman, D.R., Keely, P.J., Nowak, R.D., Mackie, T.R., Eliceiri, K.W., 2014. Computational segmentation of collagen fibers from second-harmonic generation images of breast cancer. https://doi.org/10.1117/1.JBO.19.1.016007 19, 016007. https://doi.org/10.1117/1.JBO.19.1.016007

Carey, S.P., Goldblatt, Z.E., Martin, K.E., Romero, B., Williams, R.M., Reinhart-King, C.A., 2016. Local extracellular matrix alignment directs cellular protrusion dynamics and migration through Rac1 and FAK. Integr. Biol. (Camb). 8, 821–835. https://doi.org/10.1039/C6IB00030D

Chen, X., Graham, J., Dabbah, M.A., Petropoulos, I.N., Tavakoli, M., Malik, R.A., 2017. An automatic tool for quantification of nerve fibers in corneal confocal microscopy images. IEEE Trans. Biomed. Eng. 64, 786–794. https://doi.org/10.1109/TBME.2016.2573642

Cheng, G., Zygourakis, K., 2012. Cell Migration. Compr. Physiol. 2, 2369–2392. https://doi.org/10.1002/J.2040-4603.2012.TB00467.X

Corliss, B.A., Doty, R.W., Mathews, C., Yates, P.A., Zhang, T., Peirce, S.M., 2020. REAVER: A program for improved analysis of high-resolution vascular network images. Microcirculation 27. https://doi.org/10.1111/MICC.12618

Crossley, R.M., Johnson, S., Tsingos, E., Bell, Z., Berardi, M., Botticelli, M., Braat, Q.J.S., Metzcar, J., Ruscone, M., Yin, Y., Shuttleworth, R., 2024a. Modeling the extracellular matrix in cell migration and morphogenesis: a guide for the curious biologist. Front. Cell Dev. Biol. 12, 1354132. https://doi.org/10.3389/FCELL.2024.1354132/FULL

Crossley, R.M., Johnson, S., Tsingos, E., Bell, Z., Berardi, M., Botticelli, M., Braat, Q.J.S., Metzcar, J., Ruscone, M., Yin, Y., Shuttleworth, R., 2024b. Modeling the extracellular matrix in cell migration and morphogenesis: a guide for the curious biologist. Front. Cell Dev. Biol. 12, 1354132. https://doi.org/10.3389/FCELL.2024.1354132/XML

Cui, T., Wang, T., 2025. Exact box-counting and temporal sampling algorithms for fractal dimension estimation with applications to animal behavior analysis. Results in Engineering 25, 103755. https://doi.org/10.1016/J.RINENG.2024.103755

de Vries, J.J., Laan, D.M., Frey, F., Koenderink, G.H., de Maat, M.P.M., 2023. A systematic review and comparison of automated tools for quantification of fibrous networks. Acta Biomater. 157, 263–274. https://doi.org/10.1016/J.ACTBIO.2022.12.009

Ehrbar, M., Sala, A., Lienemann, P., Ranga, A., Mosiewicz, K., Bittermann, A., Rizzi, S.C., Weber, F.E., Lutolf, M.P., 2011. Elucidating the role of matrix stiffness in 3D cell migration and remodeling. Biophys. J. 100, 284–293. https://doi.org/10.1016/J.BPJ.2010.11.082

Emami, N., Sedaei, Z., Ferdousi, R., 2021. Computerized cell tracking: Current methods, tools and challenges. Visual Informatics 5, 1–13. https://doi.org/10.1016/J.VISINF.2020.11.003

Ershov, D., Phan, M.S., Pylvänäinen, J.W., Rigaud, S.U., Le Blanc, L., Charles-Orszag, A., Conway, J.R.W., Laine, R.F., Roy, N.H., Bonazzi, D., Duménil, G., Jacquemet, G., Tinevez, J.Y., 2022. TrackMate 7: integrating state-of-the-art segmentation algorithms into tracking pipelines. Nat. Methods 19, 829–832. https://doi.org/10.1038/S41592-022-01507-1;SUBJMETA

Ford, A.J., Orbach, S.M., Rajagopalan, P., 2019. Fibroblasts stimulate macrophage migration in interconnected extracellular matrices through tunnel formation and

fiber alignment. Biomaterials 209, 88–102. https://doi.org/10.1016/J.BIOMATERIALS.2019.03.044

Friedl, P., Weigelin, B., 2008. Interstitial leukocyte migration and immune function. Nature Immunology 2008 9:9 9, 960–969. https://doi.org/10.1038/ni.f.212

Ghosh, B., Agarwal, K., 2023. Viewing life without labels under optical microscopes. Communications Biology 2023 6:1 6, 559-. https://doi.org/10.1038/s42003-023-04934-8

Gómez-De-Mariscal, E., Grobe, H., Pylvänäinen, J.W., Xénard, L., Henriques, R., Tinevez, J.Y., Jacquemet, G., 2024. CellTracksColab is a platform that enables compilation, analysis, and exploration of cell tracking data. PLoS Biol. 22, e3002740. https://doi.org/10.1371/JOURNAL.PBIO.3002740

Habanjar, O., Diab-Assaf, M., Caldefie-Chezet, F., Delort, L., 2021. 3D Cell Culture Systems: Tumor Application, Advantages, and Disadvantages. International Journal of Molecular Sciences 2021, Vol. 22, Page 12200 22, 12200. https://doi.org/10.3390/IJMS222212200

Hartman, C.D., Isenberg, B.C., Chua, S.G., Wong, J.Y., 2017. Extracellular matrix type modulates cell migration on mechanical gradients. Exp. Cell Res. 359, 361–366. https://doi.org/10.1016/J.YEXCR.2017.08.018

Hiraki, H.L., Matera, D.L., Wang, W.Y., Prabhu, E.S., Zhang, Z., Midekssa, F., Argento, A.E., Buschhaus, J.M., Humphries, B.A., Luker, G.D., Pena-Francesch, A., Baker, B.M., 2023. Fiber density and matrix stiffness modulate distinct cell migration modes in a 3D stroma mimetic composite hydrogel. Acta Biomater. 163, 378–391. https://doi.org/10.1016/J.ACTBIO.2022.09.043

Hotaling, N.A., Bharti, K., Kriel, H., Simon, C.G., 2015. DiameterJ: A validated open source nanofiber diameter measurement tool. Biomaterials 61, 327–338. https://doi.org/10.1016/J.BIOMATERIALS.2015.05.015

Jacquemet, G., Baghirov, H., Georgiadou, M., Sihto, H., Peuhu, E., Cettour-Janet, P., He, T., Perälä, M., Kronqvist, P., Joensuu, H., Ivaska, J., 2016. L-type calcium channels regulate filopodia stability and cancer cell invasion downstream of integrin signalling. Nat. Commun. 7, 13297. https://doi.org/10.1038/ncomms13297

Justus, C.R., Leffler, N., Ruiz-Echevarria, M., Yang, L. V., 2014. In vitro cell migration and invasion assays. J. Vis. Exp. https://doi.org/10.3791/51046

Kartasalo, K., Pölönen, R.P., Ojala, M., Rasku, J., Lekkala, J., Aalto-Setälä, K., Kallio, P., 2015. CytoSpectre: A tool for spectral analysis of oriented structures on cellular and subcellular levels. BMC Bioinformatics 16, 344-. https://doi.org/10.1186/S12859-015-0782-Y/TABLES/7

Kaukonen, R., Jacquemet, G., Hamidi, H., Ivaska, J., 2017. Cell-derived matrices for studying cell proliferation and directional migration in a complex 3D microenvironment. Nat. Protoc. 12, 2376–2390. https://doi.org/10.1038/NPROT.2017.107;SUBJMETA

Kluyver, T., Ragan-Kelley, B., Pérez, F., Granger, B., Bussonnier, M., Frederic, J., Kelley, K., Hamrick, J., Grout, J., Corlay, S., Ivanov, P., Avila, D., Abdalla, S., Willing, C., 2016. Jupyter Notebooks—a publishing format for reproducible computational workflows. ppap 87–90. https://doi.org/10.3233/978-1-61499-649-1-87

Lintz, M., Muñoz, A., Reinhart-King, C.A., 2017a. The Mechanics of Single Cell and Collective Migration of Tumor Cells. J. Biomech. Eng. 139. https://doi.org/10.1115/1.4035121

Lintz, M., Muñoz, A., Reinhart-King, C.A., 2017b. The Mechanics of Single Cell and Collective Migration of Tumor Cells. J. Biomech. Eng. 139, 0210051. https://doi.org/10.1115/1.4035121

Liu, P ;, Li, J ;, Chang, J ;, Hu, P ;, Sun, Y ;, Jiang, Y ;, Zhang, F ;, Shao, H, Liu, Ping, Li, Jun, Chang, Jiaxing, Hu, Pinli, Sun, Yue, Jiang, Yanan, Zhang, Fan, Shao, Haojing, 2024. Software Tools for 2D Cell Segmentation. Cells 2024, Vol. 13, Page 352 13, 352. https://doi.org/10.3390/CELLS13040352

Liu, Y., Keikhosravi, A., Mehta, G.S., Drifka, C.R., Eliceiri, K.W., 2017. Methods for Quantifying Fibrillar Collagen Alignment. Methods in Molecular Biology 1627, 429–451. https://doi.org/10.1007/978-1-4939-7113-8_28

Liu, Y.J., Le Berre, M., Lautenschlaeger, F., Maiuri, P., Callan-Jones, A., Heuzé, M., Takaki, T., Voituriez, R., Piel, M., 2015. Confinement and Low Adhesion Induce Fast Amoeboid Migration of Slow Mesenchymal Cells. Cell 160, 659–672. https://doi.org/10.1016/J.CELL.2015.01.007

Marcotti, S., Belo de Freitas, D., Troughton, L.D., Kenny, F.N., Shaw, T.J., Stramer, B.M., Oakes, P.W., 2021. A Workflow for Rapid Unbiased Quantification of Fibrillar

Feature Alignment in Biological Images. Front. Comput. Sci. 3, 745831. https://doi.org/10.3389/FCOMP.2021.745831/TEXT

Meijering, E., Dzyubachyk, O., Smal, I., 2012. Methods for Cell and Particle Tracking. Methods Enzymol. 504, 183–200. https://doi.org/10.1016/B978-0-12-391857-4.00009-4

Mierke, C.T., 2020. Cell Mechanics Drives Migration Modes. https://doi.org/10.1142/S1793048020300017 15, 1–34. https://doi.org/10.1142/S1793048020300017

Mihashi, H., Ahmed, S.F.U., Mizukami, T., Nishiwaki, T., 2014. Quantifizieren der Rissbildung mit Hilfe der Bildanalyse und deren Einfluss auf die Permeabilität / Quantification of Crack Formation Using Image Analysis and its Relationship with Permeability. Restoration of Buildings and Monuments 12, 335–348. https://doi.org/10.1515/RBM-2006-6068

Morales, X., Cortés-Domínguez, I., Ortiz-De-Solorzano, C., 2021. Modeling the Mechanobiology of Cancer Cell Migration Using 3D Biomimetic Hydrogels. Gels 2021, Vol. 7, Page 17 7, 17. https://doi.org/10.3390/GELS7010017

Morishita, K., Watanabe, K., Ichijo, H., 2019. Cell volume regulation in cancer cell migration driven by osmotic water flow. Cancer Sci. 110, 2337–2347. https://doi.org/10.1111/CAS.14079

Morrill, E.E., Tulepbergenov, A.N., Stender, C.J., Lamichhane, R., Brown, R.J., Lujan, T.J., 2016. A validated software application to measure fiber organization in soft tissue. Biomech. Model. Mechanobiol. 15, 1467–1478. https://doi.org/10.1007/S10237-016-0776-3/TABLES/1

Naba, A., 2024. Mechanisms of assembly and remodelling of the extracellular matrix. Nat. Rev. Mol. Cell Biol. 25, 865–885. https://doi.org/10.1038/S41580-024-00767-3;SUBJMETA

Nunez-Iglesias, J., Blanch, A.J., Looker, O., Dixon, M.W., Tilley, L., 2018. A new Python library to analyse skeleton images confirms malaria parasite remodelling of the red blood cell membrane skeleton. PeerJ 2018, e4312. https://doi.org/10.7717/PEERJ.4312/SUPP-2

Padhi, A., Nain, A.S., 2020. ECM in Differentiation: A Review of Matrix Structure, Composition and Mechanical Properties. Ann. Biomed. Eng. 48, 1071–1089. https://doi.org/10.1007/S10439-019-02337-7/FIGURES/3

Pally, D., Naba, A., 2024a. Extracellular Matrix Dynamics: a Key Regulator of Cell Migration across Length-Scales and Systems. Curr. Opin. Cell Biol. 86, 102309. https://doi.org/10.1016/J.CEB.2023.102309

Pally, D., Naba, A., 2024b. Extracellular matrix dynamics: A key regulator of cell migration across length-scales and systems. Curr. Opin. Cell Biol. 86, 102309. https://doi.org/10.1016/J.CEB.2023.102309

Paluch, E.K., Aspalter, I.M., Sixt, M., 2016. Focal Adhesion-Independent Cell Migration. Annu. Rev. Cell Dev. Biol. 32, 469–490. https://doi.org/10.1146/ANNUREV-CELLBIO-111315-125341/CITE/REFWORKS

Park, J.S., Kim, D.H., Kim, H.N., Wang, C.J., Kwak, M.K., Hur, E., Suh, K.Y., An, S.S., Levchenko, A., 2016. Directed migration of cancer cells guided by the graded texture of the underlying matrix. Nature Materials 2016 15:7 15, 792–801. https://doi.org/10.1038/nmat4586

Poole, J.J.A., Mostaço-guidolin, L.B., 2021. Optical Microscopy and the Extracellular Matrix Structure: A Review. Cells 2021, Vol. 10, Page 1760 10, 1760. https://doi.org/10.3390/CELLS10071760

Popović, A., Ball, N.J., Miihkinen, M., Joshi, O., Dibus, M., Ojalill, M., Pylvänäinen, J., Ivaska, J., Goult, B.T., Jacquemet, G., 2025. Filopodome proteomics identifies CCT8 as a MYO10 interactor critical for filopodia functions. bioRxiv. https://doi.org/10.64898/2025.12.03.691809

Pourjafar, M., Tiwari, V.K., 2024. Plasticity in cell migration modes across development, physiology, and disease. Front. Cell Dev. Biol. 12, 1363361. https://doi.org/10.3389/FCELL.2024.1363361/XML

Pruitt, H.C., Lewis, D., Ciccaglione, M., Connor, S., Smith, Q., Hickey, J.W., Schneck, J.P., Gerecht, S., 2020. Collagen fiber structure guides 3D motility of cytotoxic T lymphocytes. Matrix Biology 85–86, 147–159. https://doi.org/10.1016/J.MATBIO.2019.02.003

Püspöki, Z., Storath, M., Sage, D., Unser, M., 2016. Transforms and operators for directional bioimage analysis: A survey. Adv. Anat. Embryol. Cell Biol. 219, 69–93. https://doi.org/10.1007/978-3-319-28549-8_3

Ray, A., Slama, Z.M., Morford, R.K., Madden, S.A., Provenzano, P.P., 2017. Enhanced Directional Migration of Cancer Stem Cells in 3D Aligned Collagen Matrices. Biophys. J. 112, 1023–1036. https://doi.org/10.1016/J.BPJ.2017.01.007

Rickel, A.P., Sanyour, H.J., Leyda, N.A., Hong, Z., 2020. Extracellular Matrix Proteins and Substrate Stiffness Synergistically Regulate Vascular Smooth Muscle Cell Migration and Cortical Cytoskeleton Organization. ACS Appl. Bio Mater. 3, 2360–2369. https://doi.org/10.1021/ACSABM.0C00100/ASSET/IMAGES/LARGE/MT0C00100_0009.JPEG

Schick, J., Raz, E., 2022. Blebs—Formation, Regulation, Positioning, and Role in Amoeboid Cell Migration. Front. Cell Dev. Biol. 10, 926394. https://doi.org/10.3389/FCELL.2022.926394/FULL

Schindelin, J., Arganda-Carreras, I., Frise, E., Kaynig, V., Longair, M., Pietzsch, T., Preibisch, S., Rueden, C., Saalfeld, S., Schmid, B., Tinevez, J.Y., White, D.J., Hartenstein, V., Eliceiri, K., Tomancak, P., Cardona, A., 2012. Fiji: an open-source platform for biological-image analysis. Nature Methods 2012 9:7 9, 676–682. https://doi.org/10.1038/nmeth.2019

Shokouh, G.S., Magnier, B., Xu, B., Montesinos, P., 2021. Ridge Detection by Image Filtering Techniques: A Review and an Objective Analysis. Pattern Recognition and Image Analysis 31, 551–570. https://doi.org/10.1134/S1054661821030226/FIGURES/22

Slater, B., Li, J., Indana, D., Xie, Y., Chaudhuri, O., Kim, T., 2021. Transient mechanical interactions between cells and viscoelastic extracellular matrix. Soft Matter 17, 10274–10285. https://doi.org/10.1039/D0SM01911A

Socovich, A.M., Naba, A., 2019. The cancer matrisome: From comprehensive characterization to biomarker discovery. Semin. Cell Dev. Biol. 89, 157–166. https://doi.org/10.1016/J.SEMCDB.2018.06.005

Stetler-Stevenson, W.G., Yu, A.E., 2001. Proteases in invasion: matrix metalloproteinases. Semin. Cancer Biol. 11, 143–152. https://doi.org/10.1006/SCBI.2000.0365

Stringer, C., Wang, T., Michaelos, M., Pachitariu, M., 2020. Cellpose: a generalist algorithm for cellular segmentation. Nature Methods 2020 18:1 18, 100–106. https://doi.org/10.1038/s41592-020-01018-x

Theocharis, A.D., Skandalis, S.S., Gialeli, C., Karamanos, N.K., 2016. Extracellular matrix structure. Adv. Drug Deliv. Rev. 97, 4–27. https://doi.org/10.1016/J.ADDR.2015.11.001

Ulman, V., Maška, M., Magnusson, K.E.G., Ronneberger, O., Haubold, C., Harder, N., Matula, Pavel, Matula, Petr, Svoboda, D., Radojevic, M., Smal, I., Rohr, K., Jaldén, J., Blau, H.M., Dzyubachyk, O., Lelieveldt, B., Xiao, P., Li, Y., Cho, S.Y., Dufour, A.C., Olivo-Marin, J.C., Reyes-Aldasoro, C.C., Solis-Lemus, J.A., Bensch, R., Brox, T., Stegmaier, J., Mikut, R., Wolf, S., Hamprecht, F.A., Esteves, T., Quelhas, P., Demirel, Ö., Malmström, L., Jug, F., Tomancak, P., Meijering, E., Muñoz-Barrutia, A., Kozubek, M., Ortiz-De-Solorzano, C., 2017. An objective comparison of cell-tracking algorithms. Nature Methods 2017 14:12 14, 1141–1152. https://doi.org/10.1038/nmeth.4473

Vădineanu, S., Pelt, D.M., Dzyubachyk, O., Batenburg, K.J., 2024. Reducing Manual Annotation Costs for Cell Segmentation by Upgrading Low-Quality Annotations. Journal of Imaging 2024, Vol. 10, Page 172 10, 172. https://doi.org/10.3390/JIMAGING10070172

Varankar, S.S., Bapat, S.A., 2018. Migratory metrics of wound healing: A Quantification Approach for in vitro Scratch Assays. Front. Oncol. 8, 426246. https://doi.org/10.3389/FONC.2018.00633/TEXT

Vasaturo, A., Caserta, S., Russo, I., Preziosi, V., Ciacci, C., Guido, S., Rappoport, J.Z., 2012. A Novel Chemotaxis Assay in 3-D Collagen Gels by Time-Lapse Microscopy. PLoS One 7, e52251. https://doi.org/10.1371/JOURNAL.PONE.0052251

Vasudevan, J., Jiang, K., Fernandez, J.G., Lim, C.T., 2023. Extracellular matrix mechanobiology in cancer cell migration. Acta Biomater. 163, 351–364. https://doi.org/10.1016/J.ACTBIO.2022.10.016

Vecchio, D.A., Mahler, S.H., Hammig, M.D., Kotov, N.A., 2021. Structural Analysis of Nanoscale Network Materials Using Graph Theory. ACS Nano 15, 12847–12859. https://doi.org/10.1021/ACSNANO.1C04711/ASSET/IMAGES/LARGE/NN1C04711_0005.JPEG

Vicar, T., Balvan, J., Jaros, J., Jug, F., Kolar, R., Masarik, M., Gumulec, J., 2019. Cell segmentation methods for label-free contrast microscopy: Review and comprehensive comparison. BMC Bioinformatics 20, 360-. https://doi.org/10.1186/S12859-019-2880-8/TABLES/3

Vinci, M., Box, C., Eccles, S.A., 2015. Three-dimensional (3D) tumor spheroid invasion assay. J. Vis. Exp. 2015. https://doi.org/10.3791/52686

Wang, W.Y., Pearson, A.T., Kutys, M.L., Choi, C.K., Wozniak, M.A., Baker, B.M., Chen, C.S., 2018. Extracellular matrix alignment dictates the organization of focal adhesions and directs uniaxial cell migration. APL Bioeng. 2. https://doi.org/10.1063/1.5052239

Wershof, E., Park, D., Barry, D.J., Jenkins, R.P., Rullan, A., Wilkins, A., Schlegelmilch, K., Roxanis, I., Anderson, K.I., Bates, P.A., Sahai, E., 2021. A FIJI macro for quantifying pattern in extracellular matrix. Life Sci. Alliance 4. https://doi.org/10.26508/LSA.202000880

Wiggins, L., O'Toole, P.J., Brackenbury, W.J., Wilson, J., 2025. Exploring the Impact of Variability in Cell Segmentation and Tracking Approaches. Microsc. Res. Tech. 88, 716–731. https://doi.org/10.1002/JEMT.24715

Yamada, K.M., Doyle, A.D., Lu, J., 2022. Cell-3D matrix interactions: recent advances and opportunities. Trends Cell Biol. 32, 883–895. https://doi.org/10.1016/J.TCB.2022.03.002

Yamada, K.M., Sixt, M., 2019. Mechanisms of 3D cell migration. Nat. Rev. Mol. Cell Biol. 20, 738–752. https://doi.org/10.1038/S41580-019-0172-9;SUBJMETA

Yazdi, R., Khotanlou, H., 2024. A survey on automated cell tracking: challenges and solutions. Multimedia Tools and Applications 2024 83:34 83, 81511–81547. https://doi.org/10.1007/S11042-024-18697-9

Zhao, T., Huang, Y., Zhu, J., Qin, Y., Wu, H., Yu, J., Zhai, Q., Li, S., Qin, X., Wang, D., Li, T., Liu, Y., 2025. Extracellular Matrix Signaling Cues: Biological Functions, Diseases,

and Therapeutic Targets. MedComm (Beijing). 6. https://doi.org/10.1002/MCO2.70281

Zudaire, E., Gambardella, L., Kurcz, C., Vermeren, S., 2011. A Computational Tool for Quantitative Analysis of Vascular Networks. PLoS One 6, e27385. https://doi.org/10.1371/JOURNAL.PONE.0027385